Universal strategy for volumetric single-cell processing, CuRVE, and its demonstration in rapid and scalable organ-scale molecular phenotyping, eFLASH

Dae Hee Yun[1,2,7], Young-Gyun Park[2,3,7], Jae Hun Cho[4], Lee Kamentsky[2,3], Nicholas B. Evans[2,3], Nicholas DiNapoli[2,3], Katherine Xie[2,3], Seo Woo Choi[2,4], Alexandre Albanese[2,3], Yuxuan Tian[4], Chang Ho Sohn[2,3], Qiangge Zhang[5,6], Minyoung E. Kim[1,2], Justin Swaney[4], Webster Guan[4], Juhyuk Park[2-4], Gabi Drummond[1], Heejin Choi[2,3], Luzdary Ruelas[4], Guoping Feng[5,6], Kwanghun Chung*[1-4,6]

[1]Department of Brain and Cognitive Sciences
[2]Picower Institute for Learning and Memory
[3]Institute for Medical Engineering and Science
[4]Department of Chemical Engineering
[5]McGovern Institute for Brain Research
Massachusetts Institute of Technology (MIT), Cambridge, MA, USA
[6]Broad Institute of MIT and Harvard, Cambridge, MA, USA

[7]These authors contributed equally to this work.

*Correspondence should be addressed to K.C. (khchung@mit.edu).

ABSTRACT

Single-cell molecular analysis has transformed our understanding of cellular heterogeneity and cell-cell interactions within tissues. Yet, extending single-cell analysis to intact volumetric tissues to maintain organ-scale spatial information poses a significant challenge due to the difficulty in achieving uniform chemical processing of densely packed cells within volumetric tissues. Here, we introduce **C**ontin**u**ous **R**edispersion of **V**olumetric **E**quilibrium (CuRVE) in nanoporous matrices as a novel conceptual framework to address this challenge. CuRVE ensures uniform processing of all cells in organ-scale tissues by perpetually maintaining dynamic equilibrium of the tissue's gradually shifting chemical environment. We demonstrate the implementation of CuRVE through eFLASH (**e**lectrophoretic-**F**ast **L**abeling using **A**ffinity **S**weeping in **H**ydrogel), a rapid and scalable immunolabeling technology capable of labeling whole mouse and rat brains, marmoset, and human tissue blocks within just one day. With eFLASH we discovered that wildtype adult mice experience highly variable regionalized reduction of parvalbumin (PV) immunoreactive cells, a phenotype missed by the genetic labeling system commonly used for functional studies of PV neurons and their disease specific features. We envision that CuRVE and eFLASH will advance the field of volumetric single-cell processing and analysis, facilitating comprehensive single-cell level investigations within their spatial context in organ-scale tissues.

In recent years, the field of single-cell analysis has revolutionized our understanding of cellular heterogeneity and functional diversity within tissues. Scalable and automated technologies, such as flow cytometry and single-cell RNA sequencing, have provided unparalleled insights into complex biological processes by enabling the quantitative analysis of biological systems at single cell resolution, providing detailed information on cell populations and gene expression relationships[1,2]. Integration of such data with complementary techniques, including immunohistochemistry, in-situ hybridization, and spatial transcriptomic techniques is an active area of research to achieve multi-omic single cell resolution investigation with spatial context[3–5], epigenetic modifications[6,7], translational abundance[8], and post-translational modifications[9].

Single-cell analysis methods necessitate a series of multi-step chemical processing, such as fixation, labeling, and washing, to be performed on cells. Ensuring uniform chemical treatment of all cells is pivotal to attain accurate, quantitative, and comparable single-cell readouts. Conventionally, uniform treatment of cells has been achieved through tissue dissociation into

suspended cells or dissection of tissue into ultra-thin sections to facilitate direct exposure of all cells to a thoroughly mixed chemical environment[10].

Volumetric intact tissue processing and imaging has emerged as a promising approach to achieve organ-scale single-cell analysis while accurately capturing spatial contexts as well as connectivity information. Innovations in tissue clearing and tissue engineering technologies have enabled transformation of tissue into a transparent macromolecule-permeable hydrogel[11–14]. Methodologies to achieve holistic labeling of whole organs via transgenic[15] or molecular labeling approach[16–34], are also advancing rapidly. Combined with the rapidly evolving field of lightsheet microscopy[35] and AI-driven analysis, whole organs can now be imaged intact and analyzed at cellular and sub-cellular resolution.

Despite its potential, the transition of true single cell analysis from 1D (dissociated single cells) and 2D (ultra-thin tissue sections) to 3D organ-scale tissues still poses a formidable challenge. In intact mammalian organs (e.g., mouse brain), for instance, tens of millions of cells are densely packed. Even with improved permeabilization through tissue transformation, intact organs remain profoundly dense, impeding the efficient transport of necessary chemicals essential for single-cell analysis from the organ surface to its core. Only cells near the organ surface are directly exposed to a thoroughly mixed chemical environment. Consequently, cells located in different parts of the organ experience unequal chemical processing, creating disparities that compromise the comparability of obtained results. This issue mirrors the challenge encountered when attempting to merge results from differently processed batches of dissociated cells for data integration[1].

To address the fundamental challenge of volumetric single-cell processing and analysis, we introduce a novel concept termed **C**ontin**u**ous **R**edispersion of **V**olumetric **E**quilibrium (CuRVE) in nanoporous matrices. Unequal processing of cells in organ-scale tissue occurs because the chemical environment surrounding cells is spatially disturbed due to various factors such as slow chemical transport and rapid chemical reactions throughout the tissue (Fig. 1a). We hypothesized that if such spatial disturbance in chemical environment can be eliminated, perfectly uniform processing of all cells in volumetric tissues would be possible. CuRVE describes a paradigm where the change in tissue chemical reaction environment occurs at a rate slow enough to allow the redispersion of unevenly distributed chemicals, continuously, thereby maintaining chemical equilibrium tissue-wide at any given moment. By perpetually maintaining the state of such

dynamic equilibrium, the entire system can undergo chemical composition changes necessary for cell processing, while ensuring that all cells in intact tissues consistently experience the same processing conditions (Fig. 1b).

To demonstrate the value of implementing CuRVE, we focused on its implementation in organ-scale intact tissue immunolabeling, which is the most challenging among the necessary tissue processing steps for achieving high-resolution organ-scale imaging. Immunolabeling benefits from the specificity and robustness of immunoglobulins as molecular probes, however, their slow tissue penetration and high reactivity creates disparate antibody concentrations throughout the tissue volume, causing unequal chemical processing of cells and uneven labeling. The large difference between slow transport rate and fast reaction rate, along with the heterogeneous properties of both protein targets and probes, presents significant challenges in developing a practical one-size-fits-all solution. Extensive research has been done to shift the reaction-diffusion balance to facilitate deep immunolabeling including system-wide reaction inactivation and subsequent reactivation (the SWITCH concept[19]), partial reaction inhibition via specialized buffer formulation (CUBIC-HistoVision[17]), and partial reaction inhibition utilizing high temperature (ThICK/SPEARs[21]). While these methods have convincingly demonstrated organ-scale immunolabeling, realizing the full potential of CuRVE to uniformly process intact tissues will enable more efficient and versatile applications.

Here we present eFLASH (**e**lectrophoretic-**F**ast **L**abeling using **A**ffinity **S**weeping in **H**ydrogel) as a proof of concept for implementation of CuRVE in intact tissue immunolabeling. In eFLASH, we gradually change the tissue-wide chemical environment (e.g., buffer composition and antibody concentration) from inhibition of antibody binding to normal binding while maintaining tissue-wide chemical equilibrium at any given moment. In this process, electrophoretically enhanced chemical transport rapidly disperses chemicals to minimize the spatial discrepancy of chemical compositions and quickly reestablish tissue-wide equilibrium.

We first conducted computational simulation to theoretically demonstrate that CuRVE can enable superior organ-scale uniform processing of cells. Then to implement CuRVE for volumetric immunolabeling, we devised a dual sweeping of antibody binding modulators (pH and deoxycholic acid) for broadly compatible regulation of antibody reaction strength. The resulting technology we named eFLASH achieved rapid and uniform immunolabeling of intact tissue within just one day

for mouse organs, rat brains, as well as marmoset and human tissues blocks. Using eFLASH, we discovered large-scale regionalized reduction of parvalbumin immunoreactive (PV+) cells in healthy wildtype mice with significant individual and cross-hemisphere variabilities. Finally, we applied eFLASH to perform a comparative analysis between transgenic and immunological labeling that revealed discrepancies between PV-Cre/*loxP*-tdTomato double transgenic reporter line and immunological labeling of PV+ cells, establishing the importance of scalable volumetric immunolabeling for characterization of baseline proteomic expression, individual variabilities, and pathological changes.

RESULTS

Computational modeling of Continuous Redispersion of Volumetric Equilibrium (CuRVE)

To achieve volumetric processing of cells for organ-wide quantitative single-cell analysis, the chemical environment (e.g., antibody concentration) needs to be uniformly maintained throughout the tissue volume. For instance, in conventional immunolabeling methods, antibodies immediately start reacting with antigens as they are being diffused throughout a tissue. Due to the rapid consumption of antibodies compared to their dispersion rate, different parts of the tissue experience drastically different chemical environments. This issue is exacerbated in thicker tissues and results in uneven labeling and incomplete antibody penetration[20,26,36].

In immunolabeling, we hypothesized that by gradually shifting antibody-antigen binding equilibrium from a minimal binding state to a normal binding state, unevenly distributed antibodies resulting from slow diffusion and local antibody consumption could be redistributed, thereby restoring a volume-wide equilibrium before subsequent minute changes in antibody-antigen binding equilibrium occur. If this gradual adjustment of the binding equilibrium occurs at a rate that allows for the maintenance of a spatially uniform distribution of antibodies at any given moment, all cells within the intact tissue could experience the same antibody labeling conditions, thus achieving complete and uniform immunolabeling of all cells in large-scale intact tissues (Fig. 1b).

To present a proof-of-concept demonstration, we developed a computational simulation that models 1) the diffusion and conservation of antibodies, 2) dynamic equilibrium of antibodies (Ab), antigens (Ag), and their complexes (Ab-Ag), and 3) the concentration-dependent second order kinetics of Ab-Ag reaction (Supplementary Notes). We modeled the application of CuRVE under

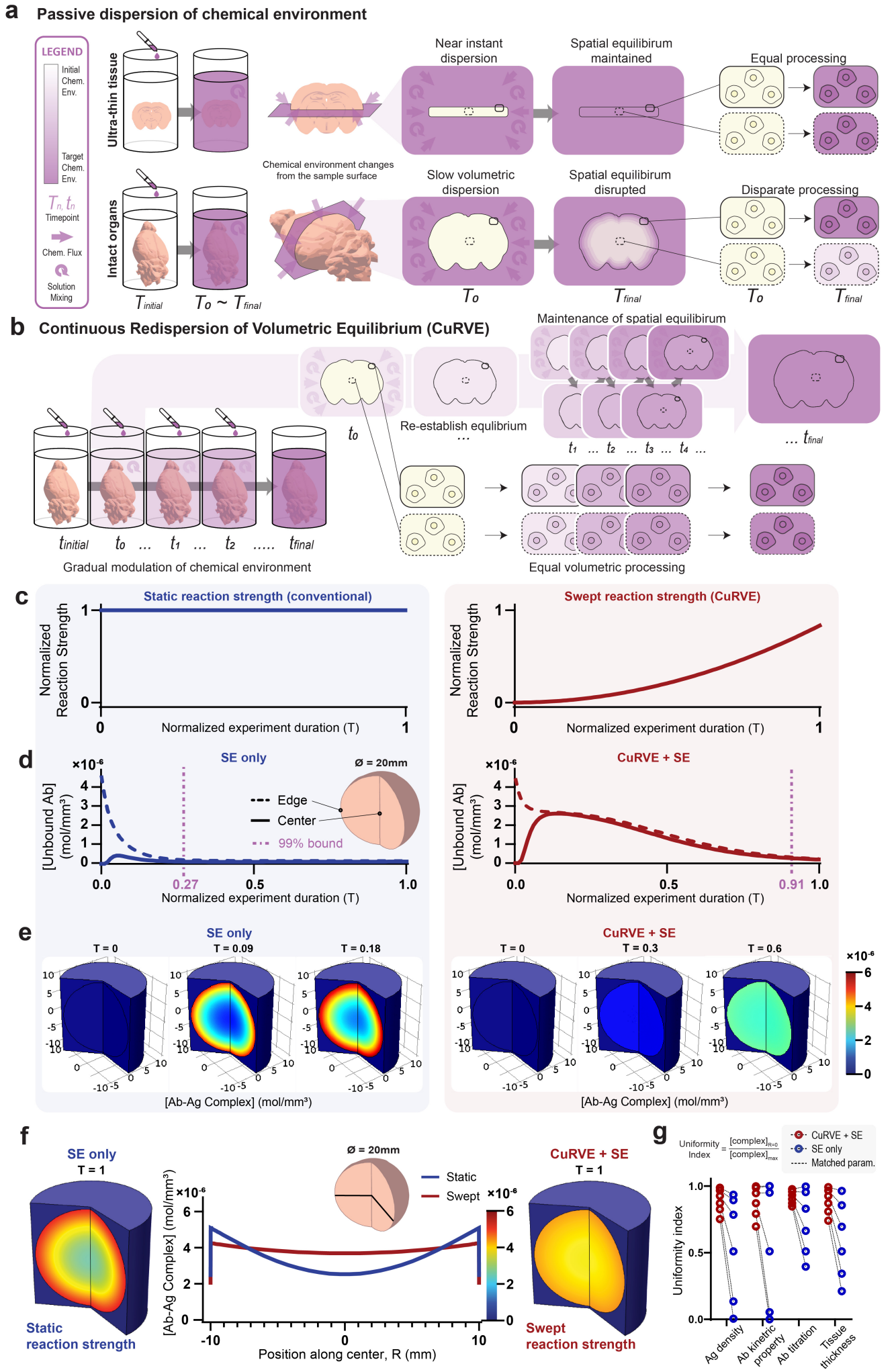

Figure 1. Conceptual description and computational modeling of CuRVE. (**a**) Schematic description comparing conventional chemical processing of ultrathin tissues and intact tissues. Ultrathin tissues experience near instant dispersion of chemical environment, allowing equal processing of all cells. Intact organs experience slow volumetric dispersion leading to disruption of spatial equilibrium and thus disparate cellular processing. (**b**) Schematic description of CuRVE for equal volumetric processing. Chemical environments are shifted gradually and allowed to re-establish equilibrium before proceeding with the subsequent gradual shift. With the continuous maintenance of spatial equilibrium, all cells can experience equal processing through the volume. (**c-g**) Computational modeling of CuRVE in COMSOL for volumetric immunolabeling. Model for conventional constant reaction methodology, static binding strength (left, blue line). Model for CuRVE, swept binding strength (right, red line). (**c**) Normalized reaction strength modulation through time. (**d**) Concentration of unbound antibodies evaluated near the surface (dotted line) and the center (solid line) throughout the simulation duration. Purple vertical dotted lines indicate the time point where 99% of the antibody-antigen complexes are formed relative to the T =1. Static, SE only (left), Swept, CuRVE + SE (right). (**e**) Concentration of antibody-antigen complexes throughout the volume represented by a color heatmap. Time points shown are relative to the 99% bound time point indicated in d. T = 0, 0.09, 0.18 for SE only. T = 0, 0.3, 0.6 for CuRVE + SE. (**f**) Overlaid concentration profiles of antibody-antigen complexes through the center of the volume at the end of the simulation. Volume rendering of the SE only model (left), and the CuRVE + SE model (right). (**g**) Sensitivity analysis via parametric sweep of antigen density, forward reaction rate, antibody to antigen ratio, and tissue thickness. The uniformity index represents the flatness of the concentration profile given by concentration at center divided by maximum concentration at T = 1. Data points evaluated with matching parameters are linked via dotted lines.

two scenarios: with simple diffusion and with stochastic electrotransport (SE). SE increases the transport rate of molecules by several orders of magnitude to enable rapid tissue processing[37], which significantly lowers the barrier for shifting the reaction-transport balance. This computational model allows for a comparative analysis between conventional static reaction strength approaches and systems implementing CuRVE. The gradual shifting of binding equilibrium required to achieve CuRVE is approximated by the sweeping of antibody reaction rate, contrasting a standard constant reaction (Fig. 1c, Extended Data Fig. 1a).

When simulating a conventional constant reaction scenario, evaluation of the unbound antibody concentration revealed that the core and the surface regions of the tissue experience vastly different antibody concentrations throughout the simulation (Fig. 1d, Extended Data Fig. 1b, Supplementary Video 1). Conversely, the use of swept reaction rate allowed the concentrations of unbound antibodies in the core and the surface to converge throughout the experiment (Fig. 1d, Extended Data Fig. 1b, Supplementary Video 1). This results in gradual and uniform formation of Ag-Ab immune complexes throughout the whole volume and throughout the experiment, as opposed to the classical propagation of the reaction front observed with the conventional approach (Fig. 1e, Extended Data Fig. 1c, Supplementary Video 1). The final concentration profiles of the immune complexes through the centerline of the volume indicates near uniform profile for the CuRVE approach compared to gradated profile of the constant reaction approach, both evaluated with identical parameters (Fig. 1f, Extended Data Fig. 1d, Supplementary Video 1). While both scenarios with simple diffusion and SE showed significant improvement of labeling uniformity, SE enabled realization of the CuRVE approach without the need for extended experimental duration. This underscores the importance of enhanced SE transport and its synergy with CuRVE.

Moreover, the CuRVE approach exhibited significantly reduced sensitivity against changes in various experimental parameters (e.g., antigen density, amount of antibody used). In general, organ-scale immunolabeling represents a complex optimization problem due to heterogeneity of tissue properties, target abundance, and probe properties[38,39]. We compared the sensitivity of both reaction modes against these variabilities through systematic simulations across wide ranges of parameters. The CuRVE configuration robustly maintained uniform labeling across the volume compared to the constant reaction mode (Fig. 1g). Further, comparing the CuRVE approach to simulations of SWITCH or partial inhibition of reaction strength (Extended Data Fig.

1e-f) revealed its potential to be especially robust against variabilities in antigen density and antibody kinetic properties (Extended Data Fig. 1g). The low sensitivity of CuRVE to experimental variables has the potential to greatly reduce the time and cost associated with the laborious optimization. Taken together, our computational model demonstrates that the implementation of CuRVE enables equal processing of all individual cells in organ-scale tissue to achieve uniform volumetric labeling across a broad range of commonly confronted experimental parameters preventing technical biases that may affect biological interpretations.

Implementation of CuRVE for ultrafast immunolabeling of organ-scale tissues

To implement CuRVE for volumetric immunolabeling, we utilized stochastic electrotransport (SE)[37] for expedited transport of chemicals. While allowing equal volumetric processing, implementing CuRVE will extend the time needed for the overall experiment. The computational modeling depicts a scenario where the swept reaction mode could take approximately three times longer to complete (Fig. 1d). Therefore, any implementation of CuRVE will benefit significantly from adopting increased transport of chemicals. Penetration of antibodies in mouse brains can take from days to weeks depending on the probe, target, and the methodology[21,40]. SE significantly accelerates dispersion of chemicals and molecular probes while preventing damage to biological tissues[37].

Next, we assessed various strategies for modulating antibody binding kinetics. Antibodies, as biological immune components, are often the most reactive in physiological conditions, and changes to pH, temperature, and ionic strength can significantly impact their binding kinetics[41]. However, due to the natural heterogeneity of antibodies, varying one factor alone is not enough to broadly regulate their kinetics. Thus, we hypothesized that combining two different modulation factors could improve the overall compatibility of the methodology. Antibody interactions can be disrupted by the presence of detergents, and we screened various chemicals for their effect on standard immunohistochemistry. Dodecylsulfuric acid is an effective antibody binding inhibitor utilized previously for discrete control of antibody binding; however, it is less suitable for gradual modulation as it strongly inhibits protein interaction even at extremely low concentrations[19,42]. Instead, deoxycholic acid, a unique bile acid with high pKa and greater polydispersity in micelle size[43,44], can modulate binding affinity of various antibodies in a concentration- and pH-dependent manner[42] (Fig. 2a-b, Extended Data Fig. 2a). Deoxycholic acid also increases the rate of antibody transport by increasing the net charge and electromobility of antibodies through cooperative

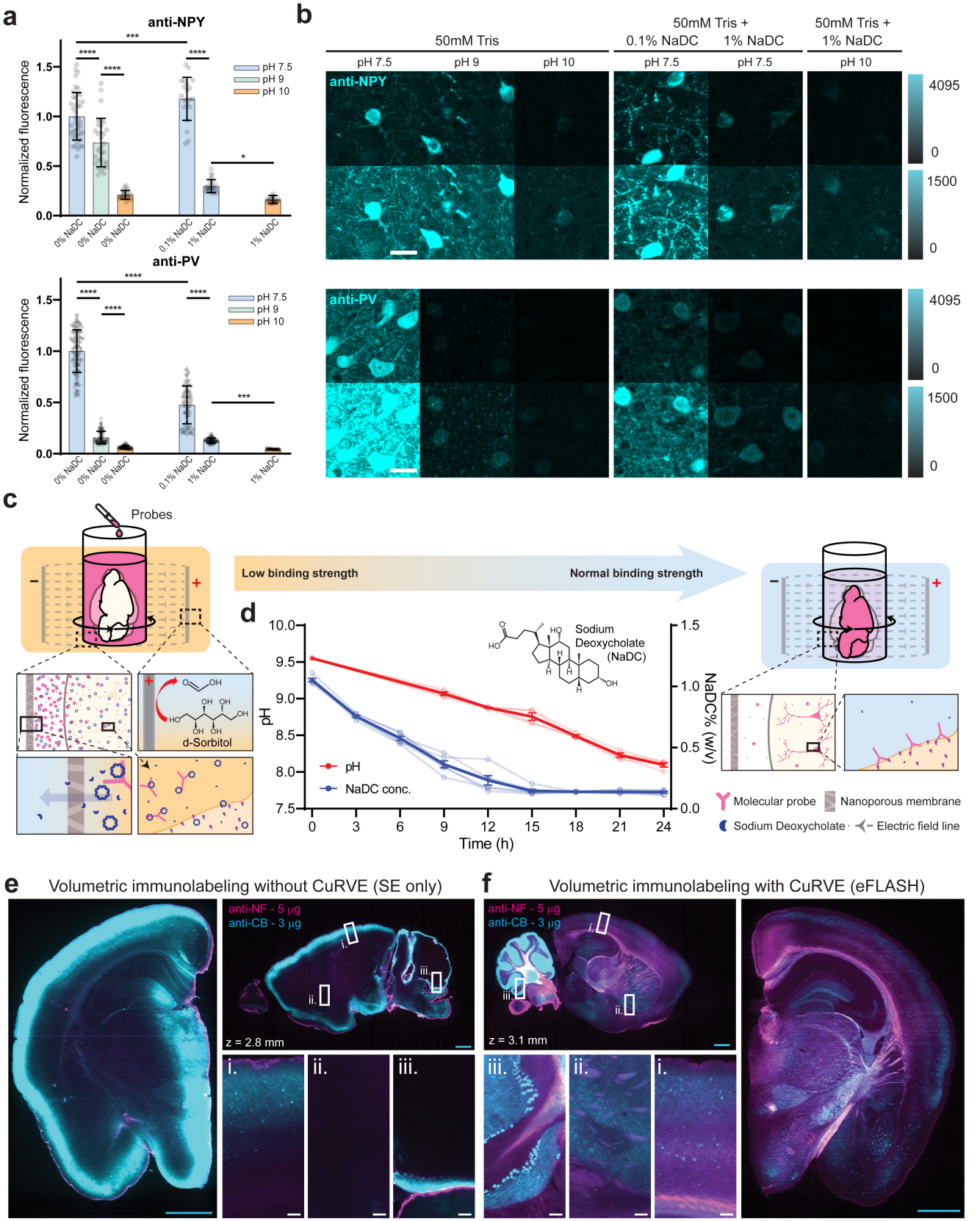

Figure 2. Design and validation of eFLASH system. (**a**) Effect of pH and sodium deoxycholate (NaDC) concentration on binding of anti-NPY and anti-PV antibodies. Normalized average soma fluorescence intensities (N = 3 independent experiments for each condition, each soma shown as an individual data point). One-Way ANOVA multiple comparisons, *P < 0.05, ***P < 0.001, ****P < 0.0001. Mean ± s.d.. (**b**) Representative images for data in **a** shown in two different display ranges. 0/4095 (top row). 0/1500 (bottom row). Scale bar = 20 µm (white). (**c**) Schematic of the eFLASH system. The pH and NaDC concentration of the labeling solution are gradually reduced to sweep the molecular probes' binding affinity from low to normal binding strength in the context of stochastic electrotransport (SE). Electrocatalytic oxidation of d-sorbitol on the anode surface generates acidic components that lower pH. NaDC concentration of the labeling solution is reduced by the diffusion of NaDC monomers through the nanoporous membrane. (**d**) Measurement of pH (N = 4 independent experiments) and NaDC concentration (N = 6 independent experiments) throughout the 24-hour processing. Mean ± s.e.m.. (**e-f**) Volumetric labeling of two hemispheres of a single brain with SE and eFLASH respectively using the same mass of antibodies: 3 µg of anti-CB (Calbindin) and 5 µg of anti-NF (Neurofilament marker). Optical plane of three-dimensional (3D) volumetric data. 20 µm max intensity projections (MIP). Sagittal (original imaging plane) and coronal (reconstructed plane). Distance of the sagittal optical plane from the medial plane (**e**) z = 2.8 mm, (**f**) z = 3.1 mm. Zoomed in view of the coronal layers (**e-i, f-i**), striatum (**e-ii, f-ii**), and cerebellum (**e-iii, f-iii**). Scale bars = 2 mm (cyan), 100 µm (white).

complex formation[45] (Extended Data Fig. 2b-c), which can further improve molecular transport. Together, these properties of deoxycholic acid render it an ideal master regulator for effectively modulating binding conditions of various antibodies for enabling CuRVE for volumetric immunolabeling.

Next, to achieve a gradual pH sweep in an automated and reproducible manner, we took advantage of electrochemical reactions that naturally occur during SE. Leveraging the electrocatalytic oxidation of D-sorbitol that produces acidic byproducts such as formic acid[46], we achieved gradual sweep of pH from 9.55 to 8.1 over the course of 24 hours in a highly reproducible and automated manner (Fig. 2c-d). To achieve a gradual modulation of the concentration of sodium deoxycholate (NaDC), the salt form of deoxycholic acid, we took advantage of the nanoporous membrane used to separate the large volume of conductive buffer and the small volume of molecular-probe-enriched labeling buffer. By carefully choosing the porosity of regenerated cellulose membrane, we achieved reproducible sweeping of NaDC concentration mediated by the diffusion of deoxycholate monomers throughout the 24-hour period (Fig. 2c), where the initial concentration of 1.05% (w/v) NaDC reduces to 0.13% (w/v) NaDC (Fig. 2d, Extended Data Fig. 2e). Furthermore, to ensure that electrocatalytic oxidation of the buffer did not affect antibody binding, we processed the eFLASH buffer and tested its initial and terminal state with 24 different antibodies, confirming strong binding in the terminal state (Extended Data Fig. 2d). We named this system eFLASH (**e**lectrophoretic-**F**ast **L**abeling using **A**ffinity **S**weeping in **H**ydrogel) as an expedited practical implementation of the CuRVE framework for volumetric immunolabeling.

Finally, to demonstrate the effectiveness of eFLASH, we stained both hemispheres from the same adult mouse brain with and without binding affinity modulation using the same amount of antibodies within 1 day (Fig. 2e-f, Supplementary Video 2). Each hemisphere is stained with 5 μg of anti-Neurofilament (NF) antibody, a pan-axonal marker, and 3 μg of anti-Calbindin (CB) antibody, an interneuron marker. SE-labeled hemisphere shows heavily gradated labeling from the surface to the center (Fig. 2e-i-iii, Supplementary Video 2), indicating antibody depletion and the necessity for significantly larger antibody quantities to improve probe penetration using the constant reaction approach. In contrast, eFLASH-labeled hemisphere shows uniform labeling of CB+ interneurons and their processes throughout the sample even with such a small amount of

antibody. This outcome is attributed to the CuRVE process effectively preventing probe depletion and ensuring equal processing of all cells within the intact sample (Fig. 2f, Supplementary Video 2). This result demonstrates the power of adopting CuRVE in combination with SE to achieve uniform, cost-effective and ultrafast labeling of large-scale tissues.

Universal applicability of eFLASH

Using eFLASH, we achieved rapid and uniform labeling of whole mouse organs, whole rat brain, marmoset brain block, as well as human cerebral organoids and human brain block while also demonstrating simultaneous labeling of three different antibodies with the same one-day immunolabeling protocol. The whole rat brain with dimensions 15.3 mm (lateral axis), 23.3 mm (A-P axis), and 11 mm (D-V axis) was uniformly labeled with anti-NeuN (Fig. 3a, Supplementary Video 3) within just one day, including densely packed populations such as hippocampal dentate granule cells (Fig. 3a-ii) and cerebellar granule cells (Fig. 3a-iv). eFLASH can uniformly label extremely densely expressed proteins such as PV (Fig. 3b, Supplementary Video 4) in challenging regions such as reticular nucleus of the thalamus (Fig. 3b-iii) and cerebellum. As a demonstration of triple volumetric immunolabeling, we performed one-shot labeling of anti-NeuN, anti-TH, and anti-ChAT, capturing all neurons and projections to dissect the dopamine- (TH) and acetylcholine- (ChAT) based diffuse modulatory systems (Fig. 3c, Supplementary Video 5), with high quality labeling that can clearly delineate populations such as the cholinergic neurons in laterodorsal tegmental nucleus and dopaminergic neurons in locus coeruleus (Fig. 3c-iii).

eFLASH is also compatible with multiple rounds of labeling, making it particularly advantages for precious samples as those derived from non-human primates and humans. We performed two separate rounds of uniform labeling on marmoset visual cortex with anti-PV (Fig. 3d) and anti-NPY (Fig. 3e, Supplementary Video 6), identifying disparate distributions for both PV+ and NPY+ neurons compared to those in mouse visual cortex. In marmoset, we observed variable distribution of PV+ cells across the visual cortical layers, contrasting with the more uniform distribution seen in mouse visual cortex (Fig. 3d-i-ii). Furthermore, NPY+ cells in the marmoset visual cortex were mostly localized to deep regions beyond layer IV and into white matter, while in the mouse cortex, anti-NPY cells were more evenly distributed across the cortical layers (Fig. 3e-i-ii).

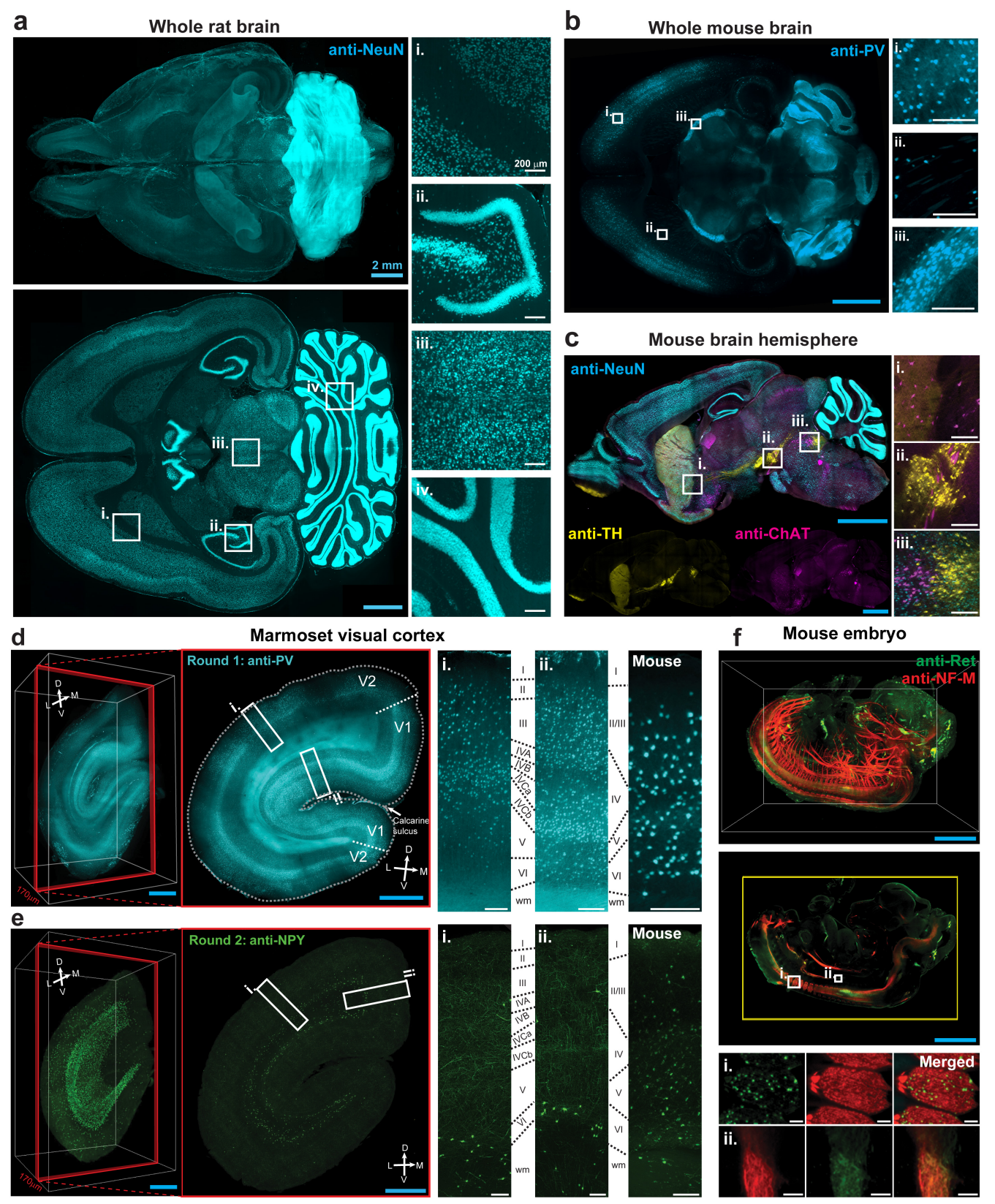

Figure 3. Rapid, uniform, and universal volumetric immunolabeling using eFLASH. (**a**) Whole volume rendering, representative optical section, and magnified images (**a-i-iv**) of whole rat brain labeled with anti-NeuN. Supplementary Video 3. (**b**) Representative optical section and magnified images (**b-i-iii**) of whole mouse brain labeled with anti-PV. Supplementary Video 4. (**c**) Representative optical section and magnified images (**c-i-iii**) of mouse brain hemisphere simultaneously labeled with anti-NeuN, anti-TH, and anti-ChAT antibodies. Supplementary Video 5. (**d-e**) Whole volume rending, representative optical section (170 μm MIP), and magnified images (**d-i-ii, e-i-ii**) of marmoset brain block containing visual cortex (5 mm x 5 mm x 8 mm) labeled with (**d**) round 1: anti-PV and (**e**) round 2: anti-NPY (round 2). Supplementary Video 6. (**f**) Whole volume rendering, representative optical section, and magnified images (**f-i-ii**) of mouse embryo labeled with anti-mouse Ret and anti-NF-M. Optical sections are 20 μm MIP unless specified otherwise. Scale bars = 2 mm (cyan), 200 μm (white).

Additionally, to demonstrate the utility of eFLASH beyond neuroscience, using one single protocol without any additional optimization besides antibody validation, we performed immunolabeling of mouse embryo (Fig. 3f), mouse intestine, mouse liver lobule, mouse lung, mouse ear canal, and mouse heart, as well as human cerebral organoid and human brain block (Extended Data Fig. 3). Altogether, we demonstrated uniform volumetric immunolabeling of various cell type specifying markers (e.g., PV, CB, CR, NPY, SST, TH, TPH2, ChAT, VIP, nNOS, NeuN, GFAP, Iba1, TBR1[47], SOX2[47] and Vimentin), structural markers (e.g., α-SMA, β-tubulin, SMI-312 (pan-axonal), Neurofilament-L, -M, and -H), neuronal activity proxy (e.g., cFos[48]), and other non-antibody molecular probes (e.g., SYTO 16 and Lectin) (Fig. 3a-f, Extended Data Fig. 4, Supplementary Table 1). Together, these results demonstrate that eFLASH is a universal platform compatible with a wide range of tissue-types and molecular probes without the need for laborious optimization procedures.

To demonstrate the versatility of eFLASH, we labeled intact tissues from mice, rats, marmosets and human organoids with 62 antibodies and 2 molecular probes. The affinity sweeping mechanism of eFLASH renders the technique robust against variabilities in tissue and antibodies properties, enabling the use of the same operational parameters for a wide range of samples. With electrophoretically enhanced molecular dispersion, eFLASH can label rodent organ-scale tissues, including whole rat brains, within just one day. Together, these results demonstrate that eFLASH is a universal platform compatible with a wide range of tissue-types and molecular probes without the need for laborious optimization procedures.

Brain-wide comparison of genetic and protein-based cell type labeling

To demonstrate the power of quantitative organ-scale immunohistological cell profiling, we utilized eFLASH to compare genetic and protein-based cell-type labeling in two widely used transgenic labeling methods: Cre-*LoxP* and BAC (Bacterial Artificial Chromosome) transgene[49–52]. Cell type marker proteins are indispensable resources for cellular phenotyping as their expression can indicate specific cell lineages or characteristic physiological functions. Transgenic lines incorporating fluorescence reporters driven by the transcription of cell type marker genes have been extensively used to investigate organ-wide distribution of distinct cell types and their disease-specific changes[51,53,54]. However, several studies have reported discrepancies between transcription activity and protein expression[55,56], known to occur due to varying degrees of leaky

expression, poor inducibility, and toxicity[51,57–59]. Differences in protein expression levels and dynamics can contribute to such variations as well[60], underscoring the importance of organ-wide immunohistochemical protein expression analysis as a suitable approach to supplement or corroborate transgenic labeling.

First, we compared genetic and antibody-based labeling of PV expressing cells, the largest class of GABAergic inhibitory neurons, in intact mouse brains. To prevent the decay of the genetically expressed fluorescent proteins, we performed SHIELD preservation, known to robustly conserve fluorescent signals[12], then employed eFLASH to immunolabel a PV-Cre[61]/*loxP*-tdTomato[62] double transgenic mouse hemisphere using an extensively validated anti-PV antibody (Fig. 4a-c). We conducted a brain-wide quantitative analysis comparing PV-tdTomato, a reporter fluorescent protein driven by the expression of parvalbumin gene, and anti-PV+ (i.e., PV immunoreactive) signals, which revealed substantial discrepancies between the two labeling approaches. For imaging processing and detection of PV-tdTomato and anti-PV cells, we utilized our image analysis pipeline[63], demonstrated on multiple cell-type markers (Extended Data Fig. 5). Interestingly, the degree of mismatches varied considerably across different brain regions (Fig. 4b-c, Supplementary Video 7). Notably, in contrast to high degree of correspondence between PV-tdTomato and anti-PV labeling in primary motor and primary somatosensory cortices (with 88% and 85% of co-positivity respectively), a substantial fraction of tdTomato-labeled cells exhibited non-detectable PV protein levels in certain cortical areas (e.g., 56% and 75% in piriform and lateral entorhinal cortex, respectively) as well as subcortical regions (45% in caudate putamen, CPu; 62% in nucleus accumbens, NAc). Furthermore, our analysis also revealed the presence of anti-PV+ populations that were not covered by genetic labeling. For example, in CPu and Nac, 66% and 77% of anti-PV+ cells, respectively, did not express detectable levels of tdTomato (Fig. 4b-c).

Next, we compared genetic and protein-based labeling of choline acetyltransferase (ChAT) expressing cells. The cholinergic system is known to have complex ChAT and vesicular acetylcholine transporter regulation which can complicate transgenic approaches to label the whole system. The ChAT^{BAC}-eGFP mice[64] has been widely used to label cholinergic neurons in both central and peripheral nervous systems. We observed significant divergence of enhanced green fluorescent protein (EGFP) expression from the ChAT immunoreactivity pattern (Fig. 4d-h, Supplementary video 8). For example, in M1 and S1 cortex, only 9% and 14% of EGFP+ cells

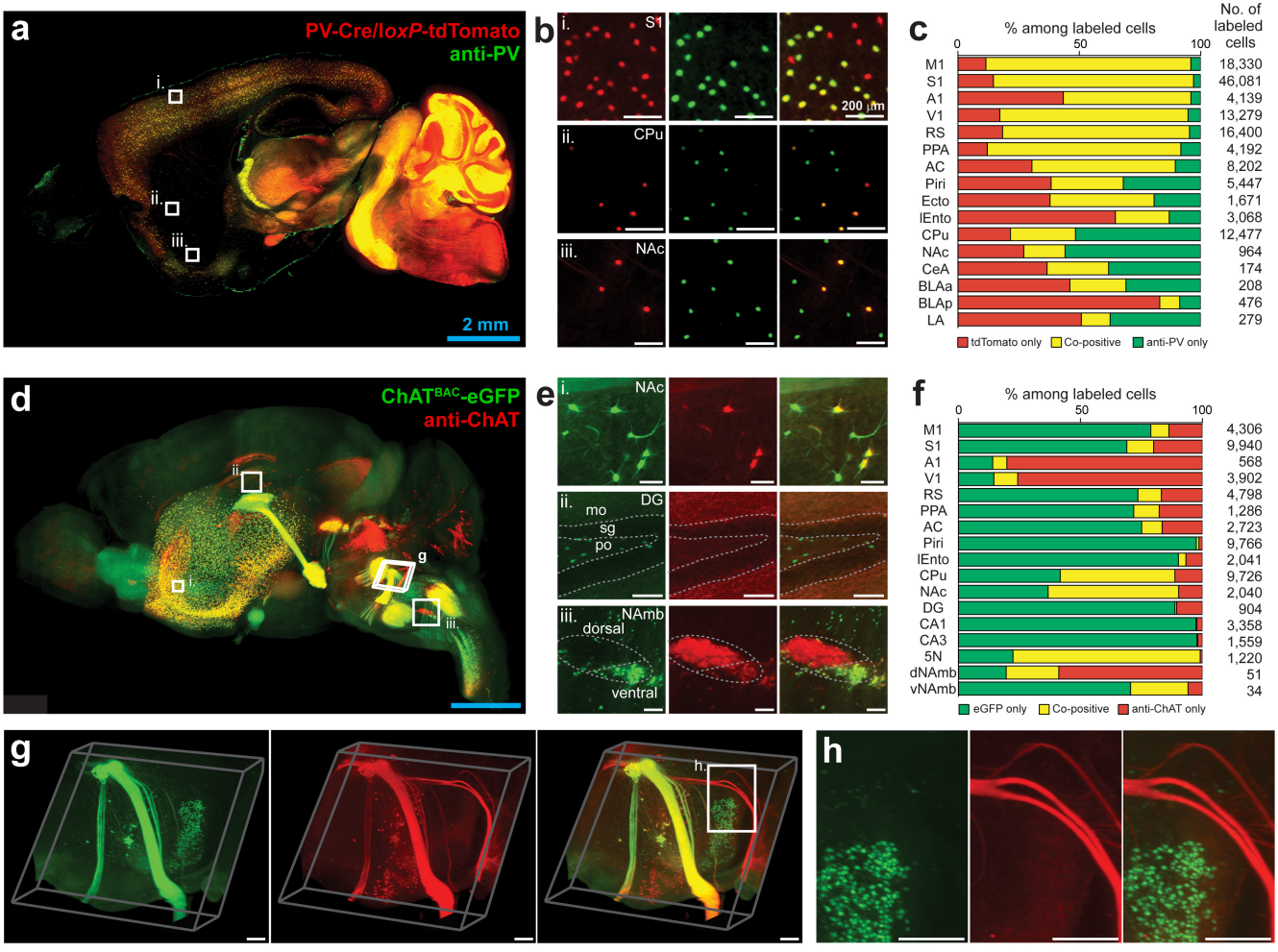

Figure 4. Holistic comparison of transgenic and immunolabeling-based cell-type labeling. (**a-c**) 3D dataset from a PV-Cre and *loxP*-tdTomato dual transgenic mouse hemisphere stained with anti-PV antibody. (**a**) Representative optical section. (**b**) Magnified images of **a**. (**c**) A percentage plot for tdTomato-only (red), anti-PV-only (green), and tdTomato and anti-PV co-positive cells (yellow) among all the labeled cells in individual representative brain regions. (**d-h**) 3D dataset of a ChAT^{BAC}-eGFP mouse brain stained with anti-ChAT antibody. (**d**) Whole volume rendering. (**e**) Magnified images of **d**. (**f**) A percentage plot for eGFP-only (green), anti-ChAT-only (red), and eGFP and anti-ChAT co-positive cells (yellow) among all the labeled cells in individual representative brain regions. (**g**) Magnified view of **d**. (**h**) Zoom-in view of **g**. Scale bars = 2 mm (cyan), 200 μm (white). M1, primary motor cortex; S1, primary somatosensory cortex; A1, primary auditory cortex; V1, primary visual cortex; RSA, retrosplenial cortex; PPA, posterior parietal association cortex; AC, anterior cingulate cortex; Piri, piriform cortex; Ecto, ectorhinal cortex; lEnto, lateral entorhinal cortex; CPu, caudoputamen; NAc, nucleus accumbens; CeA, central amygdala; BLAa, basolateral amygdala, anterior part; BLAp, basolateral amygdala, posterior part; LA, lateral amygdala; DG, dentate gyrus; mo, dentate gyrus, molecular layer; sg, dentate gyrus, granule cell layer; po, dentate gyrus, polymorph layer; CA1, hippocampal CA1; CA3, hippocampal CA3; 5N, motor nucleus of trigeminal; dNAmb, nucleus ambiguus, dorsal part; vNAmb, nucleus ambiguus, ventral part.

were also anti-ChAT+ respectively. In hippocampal CA1 and CA3, only 0.2% and 0.3% of EGFP+ cells exhibited detectable levels of ChAT immunoreactivity. Additionally, substantial populations of ChAT immunoreactive cells without EGFP expression were observed, particularly in primary auditory and visual cortices (93% and 89%, respectively) (Fig. 4f). These discrepancies were heterogeneous even within the same brain region. For instance, in the Nucleus accumbens ventral part, most anti-ChAT+ cells were also EGFP+ (80%), while in its dorsal counterpart, only 26% of anti-ChAT+ cells were colocalized with EGFP+ (Fig. 4e-iii). Furthermore, 3D visualization of the hemisphere revealed labeling mismatch in fiber bundles, where we observed a brain stem fiber bundle composed of anti-ChAT+ axons without EGFP signals (Fig. 4g-h).

The use of transgenes for protein expression profiling is a complex and nuanced topic that necessitates a comprehensive understanding of gene dynamics and expression levels. For example, despite its wide applicability, CRE-dependent genetic targeting has a possibility of false-positive (e.g., transgene-independent CRE expression), true-negative (e.g. CRE mosaicism)[58], and individually variable labeling (e.g. parental inheritance pattern)[58,65,66]. The exact strategy utilized for transgenic labeling directly influences the population of neurons labeled, and with the most commonly used transcription activation-based binary systems (e.g., Cre/*loxP* binary system), all cells expressing the target protein at any point during their development will be labeled with the reporter proteins[67]. Hence, although the discrepancies between transient target protein expression and cumulative reporter protein expression have been previously described in part, the degree of discrepancies observed brain-wide here highlights the necessity for holistic validation. These results suggest that eFLASH can enable holistic and unbiased organ-wide single-cell immuno-profiling, offering a precise and specific snapshot of endogenous protein levels, which can effectively complement and validate the transgenic labeling approach.

Significant individual variability of anti-PV+ expression in healthy wildtype mice

While investing the discrepancy between transgenic labeling and immunolabeling of PV neurons in PV-Cre[61]/*loxP*-tdTomato[62] mice, we observed significant regionalized loss of anti-PV+ neurons in both wildtype and reporter mice. Parvalbumin is a calcium-binding protein and neurons expressing PV are known to play a key role in regulating brain functions, with their disruptions associated with neuropsychiatric conditions, including schizophrenia, bipolar disorder, and autism spectrum disorders (ASD)[68]. Notably, both individuals with ASD and ASD mouse models have been reported to show reduced numbers of PV+ cells[68,69], and schizophrenia mouse models have

exhibited decreased PV immunoreactivity in the prefrontal cortex[70]. Previously, the large regionalized loss of anti-PV+ neurons has been observed and described as "parvalbumin holes" for mice with deficits in GFRa1 signaling[71], however, to our knowledge we are the first to report the observation of this phenomenon in healthy wildtype mice with holistic whole brain data. We observed this phenotype of regionalized reduction of PV, henceforth named low-PV zone (LPZ), in both eFLASH-labeled whole brains as well as in conventionally labeled tissue sections from healthy wildtype adult mice (Extended Data Fig. 6, Supplementary Video 9). For this validation, we sourced animals from three separate institutes to further control the impact of environmental variability on this phenotype.

Interestingly, high resolution confocal imaging revealed that the large regions with unusually low density of anti-PV+ somas still maintained a robust network of anti-PV+ processes as well as inhibitory synapses marked by anti-Gephyrin immunolabeling (Fig. 5a-i). However, we did observe reduction of inhibitory PV+/Gephyrin+ synapses (Extended Data Fig. 7a-c), potentially suggesting reduction of inhibitory activity in the low PV density regions. We conducted an additional round of immunolabeling of eFLASH-labeled sample using traditional passive immunohistochemistry with a different PV antibody (Fig. 5b). Signals from two different PV antibodies fully overlapped, verifying the observed discrepancy between anti-PV+ and PV-tdTomato signal in Fig. 4a-b. We also observed that PV-tdTomato signal persisted in LPZ (Extended Data Fig. 7d-e). Additionally, LPZ was not associated with loss of neuron or nuclei density, and LPZ borders were not correlated with the distribution of calbindin (CB) immunoreactive cells, another calcium-binding interneuron marker (Fig. 5c, Extended Data Fig. 7f-h, Supplementary Video 9).

To holistically characterize LPZs and compare the population of PV-tdTomato+ and anti-PV+ neurons, we conducted brain-wide phenotyping of seven age-matched P56 male PV-Cre/*loxP*-tdTomato double transgenic mice, three of which were littermates (denoted brains 1~3). We observed LPZs with extremely sparse anti-PV+ somas still had robust PV-tdTomato labeling (Fig. 5d, Supplementary Video 10), and these regions with mismatch in PV-tdTomato and anti-PV labeling were observed in all mice. We observed high individual variability in total LPZ volumes (Fig. 5f) of LPZs and their locations (Fig. 5e,g), even among littermates, often with significant lateral differences across hemispheres. Genetically labeled PV cells (tdTomato+) exhibited consistent densities across all mouse brains, and we did not observe associated changes to

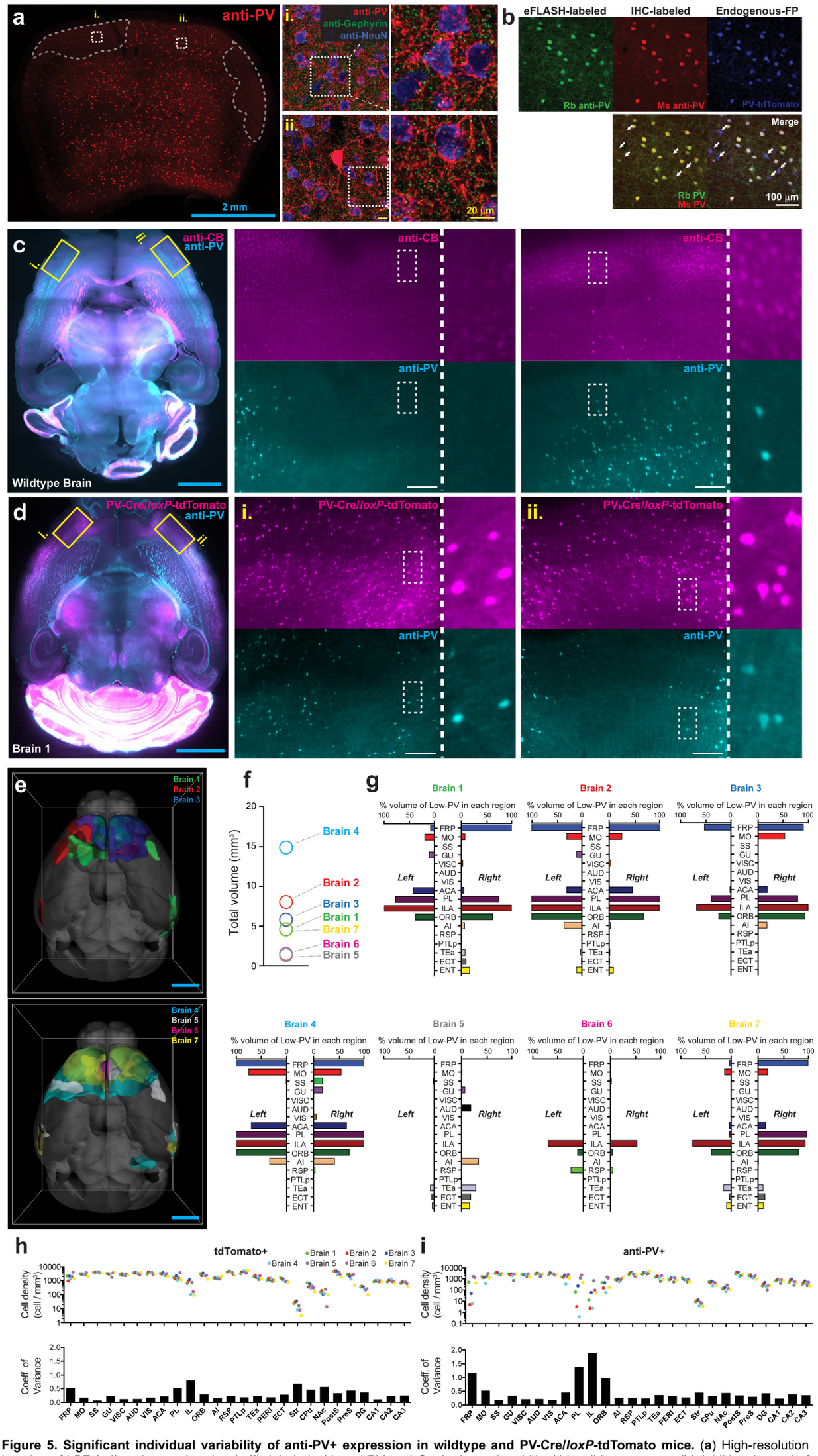

Figure 5. Significant individual variability of anti-PV+ expression in wildtype and PV-Cre/*loxP*-tdTomato mice. (**a**) High-resolution imaging of LPZ (**a-i**) and normal region (**a-ii**), labeled with anti-PV, anti-Gephyrin, and anti-NeuN in wildtype mouse. (**b**) Additional round of immunolabeling of eFLASH-labeled tissue (with rabbit host anti-PV, green) using mouse-host PV antibody (red). White arrows indicate PV-Cre/*loxP*-tdTomato expression (blue) that is disparate from both antibody labeling. (**c**) Representative optical section of wildtype mice labeled with anti-PV (cyan) and anti-CB (magenta) and representative regions with LPZ. (**c-i-ii**) with zoomed in images. (**c-i**) Seven PV-cre and loxP-tdTomato double-transgenic mouse brains were eFLASH labeled with anti-PV antibody. (**d**) Representative optical section of PV-Cre/loxP-tdTomato (magenta) mice labeled with anti-PV (cyan) and representative regions with LPZ. (**d-i-ii**) with zoomed in images. (**e**) 3D segmentation of low PV soma density regions in the seven brains. Brains 1-3 are littermates. (**f**) Total volumes of low PV regions in individual brains. (**g**) Quantification of the low PV region volumes in each brain area in the left and right hemispheres. Brain-wide quantification of PV+ cells identified based on (**h**) protein expression and (**i**) genetic fluorescent protein expression. Bottom row bar graph represents coefficient of variance for the regional densities between the seven brains. Scale bars, 2 mm (cyan), 100 μm (white), and 20 μm (yellow). 20 μm MIP optical sections. FRP, frontal pole of the cerebral cortex; MO, somatomotor areas; SS, somatosensory areas; GU, gustatory areas; VISC, visceral area; AUD, auditory areas; VIS, visual areas; ACA, anterior cingulate area; PL, prelimbic area; IL, infralimbic area; ORB, orbital area; AI, agranular insular area; RSP, retrosplenial area; PTLp, posterior parietal association area; TEa, temporal association areas; ECT, ectorhinal araea; ENT, entorhinal area; Str, striatum; CPu, caudoputamen; NAc, nucleus accumbens; PostS, postsubiculum; PreS, presubiculum; DG, dentate gyrus; CA1, hippocampal CA1; CA2, hippocampal CA2; CA3, hippocampal CA3.

tdTomtato+ somas in LPZs (Fig. 5d,h). Immunolabeled PV+ cells (anti-PV+) showed significantly reduced density with high individual variabilities in areas such as prelimbic, infralimbic, frontal pole, and the orbital regions of the cerebral cortex (Fig. 5g,i).

As the PV-Cre/*loxP*-tdTomato reporter line both captures cumulative expression of PV and amplifies neurons with low expression of PV, the observed discrepancy potentially suggests a large-scale downregulation of PV expression during mice development. Because of the high individual and lateral variability of the observed phenotype, identification through slice-based immunohistochemistry may be challenging. To interrogate disease-specific cellular and molecular changes as well as to evaluate and validate genetic tools, it is crucial to establish accurate baselines for any given animal model. Population averages can be useful for establishing such a baseline, but they cannot capture the degree of individual variabilities. This finding demonstrates the importance and the utility of scalable volumetric immunolabeling tools such as eFLASH to provide unbiased holistic high-resolution organ-wide characterizations.

DISCUSSION

In this study, we introduced **C**ontin**u**ous **R**edispersion of **V**olumetric **E**quilibrium (CuRVE) in nanoporous matrices as a conceptual framework for uniform volumetric processing. In the case of biological tissues, the uniform processing would reduce bias and ensure faithful single-cell level analyses akin to those done on dissociated cells. Because of the inherently high density of biological tissues, even with significant permeabilization, chemical processing of intact tissue often suffers from slow diffusive mass transfer. The CuRVE approach offers a solution to navigating this transport-limited regime by slowing down the reactions so that the dispersion of reactants can reestablish volumetric equilibrium at any given moment before a subsequent minute change in reaction strength occur. Both reversible and irreversible reactions will be compatible with CuRVE as long as the ratio between the reaction rate and the transport rate, essentially the Damköhler number, can be manipulated to remain low enough for a given system to achieve sufficiently uniform processing.

In the context of volumetric immunolabeling, reaction-diffusion modulation has been extensively investigated to achieve organ-scale labeling (e.g., SWITCH[19], CUBIC-HV[17], ThICK/SPEARs[21]) and other innovative methods to reduce the diffusion length achieved whole rodent body (vDISCO[25]/wildDISCO[32]) and human brain slab (ELAST[22]/mELAST[72]) immunolabeling. However,

445 further advancements in practicality, versatility, and data quality are necessary to accelerate more
446 widespread adaptation and utilization of volumetric immunolabeling by the wider research
447 community. The CuRVE framework offers a novel approach to addressing some of these
448 challenges by enhancing the efficiency and flexibility of labeling techniques. Here, we
449 demonstrated eFLASH as a proof-of-concept implementation of CuRVE for an ultrafast, versatile,
450 and scalable immunolabeling of organ-scale tissues. The increased throughput, scalability, low
451 reagent requirement of eFLASH is not mutually exclusive to other technologies if the tissue can
452 withstand electrophoresis, offering options for orthogonal optimizations and improving equal
453 processing of all cells.
454
455 Our discovery of large regionalized loss of parvalbumin-immunoreactive neurons in healthy adult
456 mice with high individual variability emphasizes the importance of holistic and unbiased
457 phenotyping. In mouse adolescence, PV expression in prefrontal cortex is known to substantially
458 increase and last to adulthood[73,74], and loss of PV expression in prefrontal cortex is associated
459 with neurodegenerative models[68–70]. As we observed robust presence of PV immunoreactive
460 processes in LPZs (Fig. 5a), it is still possible that overall activity of PV expressing synapses may
461 remain high; however, the absence of PV expressing neuronal bodies at such a large-scale in
462 healthy wild type animals challenges existing preconceptions about transience of neuronal cell
463 types and developmental neurobiology.
464
465 Future applications of eFLASH reside on multiple fronts. Multiplexed proteomic investigation
466 remains a great challenge, especially in organ-scale tissues. Towards that end, the use of oligo-
467 nucleotide conjugated antibodies offers great promise by taking advantage of the combinatorial
468 barcoding capabilities as well as rapid and reliable probe exchange[75,76]. The superior throughput
469 and probe-insensitive nature of eFLASH will be a great asset for one-shot delivery and labeling
470 with a large library of oligo-conjugated antibodies for realizing highly multiplexed spatial
471 proteomics. The capacity of eFLASH to enable rapid delivery of bulkier alternative dyes such as
472 tandem fluorescent dyes, quantum dots, and Raman-dyes[36] also holds possibilities for higher
473 multiplexed molecular profiling of organ-scale tissues beyond the limited multi-color imaging
474 barrier of conventional fluorescent dyes. Furthermore, there is a lot of room for optimization to
475 speed up the process even further, which may be necessary for highly multiplexed organ-scale
476 proteomics.
477

We have demonstrated eFLASH here with SHIELD-processed tissues for its robust preservation of endogenous fluorescent protein signals. One immediate limitation is that the use of eFLASH with other types of tissue preparation may first require additional optimizations and validations. eFLASH also shares the limitation of all immunolabeling applications that rely on the accuracy, quality, and availability of commercial antibodies. Application of eFLASH on extremely large samples such as macaque or human brain sized tissue may require additional innovations to ensure adequate dissipation of heat caused by joule heating under electrophoresis. Finally, eFLASH requires the use of specialized SE equipment to manage electrophoresis and cooling; however, commercial instruments are already available with batch processing capabilities.

The newly introduced tissue processing paradigm of CuRVE approaches the challenge of volumetric processing with a new perspective that focuses on enabling equal processing of all cells throughout the volume for organ-scale quantitative single-cell analysis while maintaining their spatial contexts. With eFLASH, we demonstrated that rapid and uniform immunolabeling is possible for organs as large as a whole rat brain within only one day. With the discovery of the LPZs, we demonstrated the necessity of holistic and unbiased phenotyping that is cost-effective and scalable to a large number of samples to challenge our pre-existing assumptions. We envision that the efficiency and scalability of eFLASH will be pivotal in establishing high quality resources on baseline proteomic expression for evaluation of transgenic and pathological mammalian models as well as human clinical samples.

Acknowledgements

The authors thank the entire Chung laboratory for support and discussions. We acknowledge N. Peat for contribution to chemical screening for buffer development, L. Ochoa for discussions on transgenic mouse lines, and J. Zeng for experimental support. K.C. was supported by the Burroughs Wellcome Fund Career Awards at the Scientific Interface, Searle Scholars Program. Packard award in Science and Engineering, NARSAD Young Investigator Award, and the McKight Foundation Technology Award. This work was supported by the JPB Foundation (PIIF and PNDRF), the NCSOFT Cultural Foundation, and the NIH (1-DP2-ES027992, U01MH117072). J.P. was supported by postdoctoral fellowships from the Picower Institute of Learning and Memory.

Author Contributions

DH.Y., Y-G.P., and K.C. ideated the concept of CuRVE, designed the experiments, and wrote the manuscript with input from other authors. DH.Y. and K.C. designed eFLASH protocols and systems with help from J.C. on the initial prototype. DH.Y. performed the volumetric tissue clearing and labeling with N.D.'s assistance. Y-G.P. aided the development of the eFLASH technology by performing passive staining experiments for screening antibodies and buffers, and imaging eFLASH-labeled samples. Y-G.P. led SHIELD-processing of all tissue samples with help from K.X. and J.P.. G.F. and K.C. initiated the marmoset brain mapping project. G.F. provided the marmoset and Q.Z. perfused the marmoset. L.K., M.K. and J.S. developed the computational pipeline with Y-G.P., DH.Y., W.G., and K.C.'s input. N.B.E. and Y-G.P. performed light-sheet imaging with H.C.'s help. DH.Y. performed the computational modeling in Figure 1 with S.C.'s assistance. DH.Y. performed the buffer characterization in Figure 2. A.A. provided and imaged the SHIELD processed cerebral organoid for Figure 3. Y-G.P. and L.K. performed brain-wide cell-type mapping in Figure 4 with help from DH.Y. and K.X.. Y-G.P. performed cell-detection and LPZ analysis in Figure 5. C.S. aided in antibody and fluorescent dye screening for the project. G.D. and Y.T. helped with initial manuscript preparation. Y.T., and L.R. aided in detergent and buffer screening and characterization, including antibody electromobility measurements.

Competing interests

K.C. and J.C. are co-inventors on patents owned by MIT covering the SE technology. K.C. is a cofounder of LifeCanvas Technologies, a startup that provides solutions for 3D tissue processing and analysis.

REFERENCES

1. Stuart, T. & Satija, R. Integrative single-cell analysis. *Nature Reviews Genetics 2019 20:5* **20**, 257–272 (2019).
2. McKinnon, K. M. Flow Cytometry: An Overview. *Curr Protoc Immunol* **120**, 5.1.1-5.1.11 (2018).
3. Longo, S. K., Guo, M. G., Ji, A. L. & Khavari, P. A. Integrating single-cell and spatial transcriptomics to elucidate intercellular tissue dynamics. *Nature Reviews Genetics 2021 22:10* **22**, 627–644 (2021).
4. McGinnis, L. M., Ibarra-Lopez, V., Rost, S. & Ziai, J. Clinical and research applications of multiplexed immunohistochemistry and in situ hybridization. *J Pathol* **254**, 405–417 (2021).
5. Byron, S. A., Van Keuren-Jensen, K. R., Engelthaler, D. M., Carpten, J. D. & Craig, D. W. Translating RNA sequencing into clinical diagnostics: opportunities and challenges. *Nature Reviews Genetics 2016 17:5* **17**, 257–271 (2016).
6. Liu, H. *et al.* DNA methylation atlas of the mouse brain at single-cell resolution. *Nature 2021 598:7879* **598**, 120–128 (2021).
7. Yao, Z. *et al.* A transcriptomic and epigenomic cell atlas of the mouse primary motor cortex. *Nature 2021 598:7879* **598**, 103–110 (2021).
8. Schwanhüusser, B. *et al.* Global quantification of mammalian gene expression control. *Nature* **473**, 337–342 (2011).
9. Prabakaran, S., Lippens, G., Steen, H. & Gunawardena, J. Post-translational modification: nature's escape from genetic imprisonment and the basis for dynamic information encoding. *Wiley Interdiscip Rev Syst Biol Med* **4**, 565–583 (2012).
10. Moffitt, J. R., Lundberg, E. & Heyn, H. The emerging landscape of spatial profiling technologies. *Nature Reviews Genetics 2022 23:12* **23**, 741–759 (2022).
11. Chung, K. *et al.* Structural and molecular interrogation of intact biological systems. *Nature* **497**, 332–337 (2013).
12. Park, Y.-G. G. *et al.* Protection of tissue physicochemical properties using polyfunctional crosslinkers. *Nat Biotechnol* **37**, 73 (2019).
13. Susaki, E. A. *et al.* Whole-brain imaging with single-cell resolution using chemical cocktails and computational analysis. *Cell* **157**, 726–739 (2014).
14. Renier, N. *et al.* IDISCO: A simple, rapid method to immunolabel large tissue samples for volume imaging. *Cell* **159**, 896–910 (2014).
15. Arias, A., Manubens-Gil, L. & Dierssen, M. Fluorescent transgenic mouse models for whole-brain imaging in health and disease. *Front Mol Neurosci* **15**, (2022).
16. Renier, N. *et al.* Mapping of Brain Activity by Automated Volume Analysis of Immediate Early Genes. *Cell* **165**, 1789–1802 (2016).
17. Susaki, E. A. *et al.* Versatile whole-organ/body staining and imaging based on electrolyte-gel properties of biological tissues. *Nature Communications 2020 11:1* **11**, 1–22 (2020).
18. Zhao, S. *et al.* Cellular and Molecular Probing of Intact Human Organs. *Cell* **180**, 796-812.e19 (2020).

19. Murray, E. *et al.* Simple, Scalable Proteomic Imaging for High-Dimensional Profiling of Intact Systems. *Cell* **163**, 1500–1514 (2015).
20. Cai, R. *et al.* Panoptic imaging of transparent mice reveals whole-body neuronal projections and skull–meninges connections. *Nature Neuroscience 2018 22:2* **22**, 317–327 (2018).
21. Lai, H. M. *et al.* Antibody stabilization for thermally accelerated deep immunostaining. *Nature Methods 2022 19:9* **19**, 1137–1146 (2022).
22. Ku, T. *et al.* Elasticizing tissues for reversible shape transformation and accelerated molecular labeling. *Nature Methods 2020 17:6* **17**, 609–613 (2020).
23. Tainaka, K. *et al.* Whole-body imaging with single-cell resolution by tissue decolorization. *Cell* **159**, 911–924 (2014).
24. Belle, M. *et al.* Tridimensional Visualization and Analysis of Early Human Development. *Cell* **169**, 161-173.e12 (2017).
25. Cai, R. *et al.* Panoptic imaging of transparent mice reveals whole-body neuronal projections and skull–meninges connections. *Nature Neuroscience 2018 22:2* **22**, 317–327 (2018).
26. Lai, H. M. *et al.* Next generation histology methods for three-dimensional imaging of fresh and archival human brain tissues. *Nature Communications 2018 9:1* **9**, 1–12 (2018).
27. Tainaka, K. *et al.* Whole-body imaging with single-cell resolution by tissue decolorization. *Cell* **159**, 911–924 (2014).
28. Hama, H. *et al.* ScaleS: an optical clearing palette for biological imaging. *Nature Neuroscience 2015 18:10* **18**, 1518–1529 (2015).
29. Gleave, J. A., Lerch, J. P., Henkelman, R. M. & Nieman, B. J. A Method for 3D Immunostaining and Optical Imaging of the Mouse Brain Demonstrated in Neural Progenitor Cells. *PLoS One* **8**, e72039 (2013).
30. Sillitoe, R. V. & Hawkes, R. Whole-mount immunohistochemistry: A high-throughput screen for patterning defects in the mouse cerebellum. *Journal of Histochemistry and Cytochemistry* **50**, 235–244 (2002).
31. Dent, J. A., Polson, A. G. & Klymkowsky, M. W. A whole-mount immunocytochemical analysis of the expression of the intermediate filament protein vimentin in Xenopus. *Development* **105**, 61–74 (1989).
32. Mai, H. *et al.* Whole-body cellular mapping in mouse using standard IgG antibodies. *Nature Biotechnology 2023* 1–11 (2023) doi:10.1038/s41587-023-01846-0.
33. Kubota, S. I. *et al.* Whole-Body Profiling of Cancer Metastasis with Single-Cell Resolution. *Cell Rep* **20**, 236–250 (2017).
34. Li, W., Germain, R. N. & Gerner, M. Y. Multiplex, quantitative cellular analysis in large tissue volumes with clearing-enhanced 3D microscopy (Ce3D). *Proc Natl Acad Sci U S A* **114**, E7321–E7330 (2017).
35. Dean, K. M., Roudot, P., Welf, E. S., Danuser, G. & Fiolka, R. Deconvolution-free Subcellular Imaging with Axially Swept Light Sheet Microscopy. *Biophys J* **108**, 2807–2815 (2015).

36. Shi, L. *et al.* Highly-multiplexed volumetric mapping with Raman dye imaging and tissue clearing. *Nature Biotechnology 2021 40:3* **40**, 364–373 (2021).
37. Kim, S.-Y. *et al.* Stochastic electrotransport selectively enhances the transport of highly electromobile molecules. *Proceedings of the National Academy of Sciences* **112**, E6274–E6283 (2015).
38. Pavlova, I. P., Shipley, S. C., Lanio, M., Hen, R. & Denny, C. A. Optimization of immunolabeling and clearing techniques for indelibly-labeled memory traces. *Hippocampus* **28**, 523 (2018).
39. Yau, C. N. *et al.* Principles of deep immunohistochemistry for 3D histology. *Cell Reports Methods* **3**, (2023).
40. Murakami, T. C. *et al.* A three-dimensional single-cell-resolution whole-brain atlas using CUBIC-X expansion microscopy and tissue clearing. *Nat Neurosci* **21**, 625–637 (2018).
41. Roberts, D. *et al.* Specific ion and buffer effects on protein-protein interactions of a monoclonal antibody. *Mol Pharm* **12**, 179–193 (2015).
42. Qualtiere, L. F., Anderson, A. G. & Meyers, P. Effects of Ionic and Nonionic Detergents on Antigen-Antibody Reactions. *The Journal of Immunology* **119**, 1645–1651 (1977).
43. Cabral, D. J., Hamilton, J. A. & Small, D. M. The ionization behavior of bile acids in different aqueous environments. *J Lipid Res* **27**, 334–343 (1987).
44. Esposito, G., Giglio, E., Pavel, N. V. & Zanobi, A. Size and shape of sodium deoxycholate micellar aggregates. *Journal of physical chemistry* **91**, 356–362 (1987).
45. Makino, S., Reynolds, J. A. & Tanford, C. The binding of deoxycholate and Triton X 100 to proteins. *Journal of Biological Chemistry* **248**, 4926–4932 (1973).
46. Proença, L. *et al.* Electrocatalytic oxidation of d-sorbitol on platinum in acid medium: analysis of the reaction products. *Journal of Electroanalytical Chemistry* **432**, 237–242 (1997).
47. Albanese, A. *et al.* Multiscale 3D phenotyping of human cerebral organoids. *Scientific Reports 2021 10:1* **10**, 1–17 (2020).
48. Roy, D. S. *et al.* Brain-wide mapping reveals that engrams for a single memory are distributed across multiple brain regions. *Nature Communications 2022 13:1* **13**, 1–16 (2022).
49. Muzumdar, M. D., Tasic, B., Miyamichi, K., Li, L. & Luo, L. A global double-fluorescent Cre reporter mouse. *genesis* **45**, 593–605 (2007).
50. Livet, J. *et al.* Transgenic strategies for combinatorial expression of fluorescent proteins in the nervous system. *Nature* **450**, 56–62 (2007).
51. Gong, S. *et al.* A gene expression atlas of the central nervous system based on bacterial artificial chromosomes. *Nature* **425**, 917–925 (2003).
52. Valjent, E., Bertran-Gonzalez, J., Hervé, D., Fisone, G. & Girault, J.-A. Looking BAC at striatal signaling: cell-specific analysis in new transgenic mice. *Trends Neurosci* **32**, 538–547 (2009).
53. Kim, Y. *et al.* Brain-wide Maps Reveal Stereotyped Cell-Type-Based Cortical Architecture and Subcortical Sexual Dimorphism. *Cell* **171**, 456-469.e22 (2017).

54. Zhang, C. *et al.* A platform for stereological quantitative analysis of the brain-wide distribution of type-specific neurons. *Sci Rep* **7**, 14334 (2017).
55. Tanahira, C. *et al.* Parvalbumin neurons in the forebrain as revealed by parvalbumin-Cre transgenic mice. *Neurosci Res* **63**, 213–223 (2009).
56. Nigro, M. J., Kirikae, H., Kjelsberg, K., Nair, R. R. & Witter, M. P. Not All That Is Gold Glitters: PV-IRES-Cre Mouse Line Shows Low Efficiency of Labeling of Parvalbumin Interneurons in the Perirhinal Cortex. *Front Neural Circuits* **15**, (2021).
57. Li, X. *et al.* Generation of a whole-brain atlas for the cholinergic system and mesoscopic projectome analysis of basal forebrain cholinergic neurons. *Proc Natl Acad Sci U S A* **115**, 415–420 (2018).
58. Heffner, C. S. *et al.* Supporting conditional mouse mutagenesis with a comprehensive cre characterization resource. *Nat Commun* **3**, 1218 (2012).
59. von Engelhardt, J., Eliava, M., Meyer, A. H., Rozov, A. & Monyer, H. Functional Characterization of Intrinsic Cholinergic Interneurons in the Cortex. *Journal of Neuroscience* **27**, 5633–5642 (2007).
60. Vogel, C. & Marcotte, E. M. Insights into the regulation of protein abundance from proteomic and transcriptomic analyses. *Nat Rev Genet* **13**, 227–232 (2012).
61. Madisen, L. *et al.* A robust and high-throughput Cre reporting and characterization system for the whole mouse brain. *Nature Neuroscience 2009 13:1* **13**, 133–140 (2009).
62. Luo, L. *et al.* Optimizing Nervous System-Specific Gene Targeting with Cre Driver Lines: Prevalenceof Germline Recombination and Influencing Factors. *Neuron* **106**, 37 (2020).
63. Swaney, J. *et al.* Scalable image processing techniques for quantitative analysis of volumetric biological images from light-sheet microscopy. *bioRxiv* 576595 (2019) doi:10.1101/576595.
64. Tallini, Y. N. *et al.* BAC transgenic mice express enhanced green fluorescent protein in central and peripheral cholinergic neurons. *Physiol Genomics* **27**, 391–397 (2006).
65. Schmidt-Supprian, M. & Rajewsky, K. Vagaries of conditional gene targeting. *Nature Immunology 2007 8:7* **8**, 665–668 (2007).
66. Matthaei, K. I. & Matthaei, K. I. Genetically manipulated mice: a powerful tool with unsuspected caveats. *J Physiol* **582**, 481–488 (2007).
67. Huang, Z. J., Taniguchi, H., He, M. & Kuhlman, S. Genetic labeling of neurons in mouse brain. *Cold Spring Harb Protoc* **2014**, 150–60 (2014).
68. Marín, O. Interneuron dysfunction in psychiatric disorders. *Nature Reviews Neuroscience 2012 13:2* **13**, 107–120 (2012).
69. Zikopoulos, B. & Barbas, H. Altered neural connectivity in excitatory and inhibitory cortical circuits in autism. *Front Hum Neurosci* **7**, (2013).
70. Niwa, M. *et al.* Knockdown of DISC1 by in utero gene transfer disturbs postnatal dopaminergic maturation in the frontal cortex and leads to adult behavioral deficits. *Neuron* **65**, 480–489 (2010).
71. Canty, A. J. *et al.* Regionalized Loss of Parvalbumin Interneurons in the Cerebral Cortex of Mice with Deficits in GFRα1 Signaling. *Journal of Neuroscience* **29**, 10695–10705 (2009).

72. Park, J. *et al.* Integrated platform for multiscale molecular imaging and phenotyping of the human brain. *Science* **384**, eadh9979 (2024).
73. Caballero, A., Flores-Barrera, E., Cass, D. K. & Tseng, K. Y. Differential regulation of parvalbumin and calretinin interneurons in the prefrontal cortex during adolescence. *Brain Struct Funct* **219**, 395–406 (2014).
74. Caballero, A., Flores-Barrera, E., Thomases, D. R. & Tseng, K. Y. Downregulation of parvalbumin expression in the prefrontal cortex during adolescence causes enduring prefrontal disinhibition in adulthood. *Neuropsychopharmacology 2020 45:9* **45**, 1527–1535 (2020).
75. Black, S. *et al.* CODEX multiplexed tissue imaging with DNA-conjugated antibodies. *Nat Protoc* **16**, 3802 (2021).
76. Hong, F. *et al.* Thermal-plex: fluidic-free, rapid sequential multiplexed imaging with DNA-encoded thermal channels. *Nature Methods 2023 21:2* **21**, 331–341 (2023).
77. Lancaster, M. A. & Knoblich, J. A. Generation of cerebral organoids from human pluripotent stem cells. *Nat Protoc* **9**, 2329–2340 (2014).
78. Mellios, N. *et al.* MeCP2-regulated miRNAs control early human neurogenesis through differential effects on ERK and AKT signaling. *Molecular Psychiatry 2017 23:4* **23**, 1051 (2017).
79. Tehrani-Bagha, A. R. & Holmberg, K. Solubilization of Hydrophobic Dyes in Surfactant Solutions. *Materials* **6**, 580 (2013).
80. Podgorski, K., Terpetschnig, E., Klochko, O. P., Obukhova, O. M. & Haas, K. Ultra-Bright and -Stable Red and Near-Infrared Squaraine Fluorophores for In Vivo Two-Photon Imaging. *PLoS One* **7**, e51980 (2012).
81. Dong, H. *The Allen Reference Atlas: A Digital Color Brain Atlas of the C57Bl/6J Male Mouse.* (2008).
82. Klein, S., Staring, M., Murphy, K., Viergever, M. A. & Pluim, J. elastix: A Toolbox for Intensity-Based Medical Image Registration. *IEEE Trans Med Imaging* **29**, 196–205 (2010).

ONLINE METHODS

Mice. Young adult (2-4 month) C57BL/6 mice were housed in a 12-hour light/dark cycle with unrestricted access to food and water. All experimental protocols were approved by the MIT Institutional Animal Care and Use Committee and the Division of Comparative Medicine and were in accordance with guidelines from the National Institute of Health. The following transgenic lines were used for this study: ChAT^{BAC}-eGFP (Jackson Stock No. 007902), PV-Cre / loxP-tdTomato double hemizygous (B6 Pvalb-IRES-Cre, Jackson Strain#017320 and Ai14, Jackson Strain#007914). For LPZ validation, PFA-perfused brains of young adult (8-10 week) mice were sourced from UCSD and Hilltop Lab Animals, Inc. (Scottdale, PA).

Rat. PFA-perfused whole brains of CVF Sprague-Dawley rat weanlings were purchased from Hilltop Lab Animals, Inc. (Scottdale, PA).

Marmoset. All animal experiments were approved by the Institutional Animal Care and Use Committee of Massachusetts Institute of Technology and were performed under the guidelines from the National Institute of Health. Adult common marmosets (2-4 years old) were housed in AAALAC-accredited facilities. The housing room was maintained at 74.0 ± 2.0°F (23.3 ± 1.1°C), in the relative humidity of 50±20%, and in a 12-hour light/dark cycle. The animals were housed in dedicated cages with enrichment devices and had unrestricted access to food and water. For histological examinations, the animals were deeply sedated by intramuscular injection of Ketamine (20-40 mg/kg) or Alfaxalone (5-10 mg/kg), followed by intravenous injection of sodium pentobarbital (10-30 mg/kg). When pedal withdrawal reflex was eliminated and/or respiratory rate was diminished, animals were perfused transcardially with 0.5 mL 1000 IU/mL heparin and 100-200 ml cold PBS by gravity. Then the descending aorta of the animals was clamped, and a peristaltic pump was used to infuse another 200-300 mL ice-cold SHIELD perfusion solution (10% (w/v) GE38 and 4% PFA (w/v) in PBS). Brains were removed from the skulls and SHIELD-processed (see the section "SHIELD processing").

Organoids. Organoids were grown according to the protocol by Lancaster et al.[77], with the addition of dual SMAD inhibition between d6 and d9 to increase neural differentiation as previously described[78]. Organoids were grown from iPSC cells (System Biosciences, #SC101A-1). After Matrigel droplet embedding, organoids were transferred to 60 mm suspension culture

dishes (Corning, #430589) and placed on shaker at 75 rpm on day 16. The organoids were SHIELD-processed on day 35 (see the section "SHIELD processing").

Sodium Deoxycholate (NaDC) concentration measurement. The concentration of surfactants can be measured by the degree of solubilization of hydrophobic organic dyes. Above the critical micelle concentration, the amount of solubilized dye increases linearly with the increase in surfactant concentration[79]. Degree of solubilization was measured based on light absorption using a spectrophotometer (SM1100 Economic UV-VIS Spectrophotometer, Azzota) at 592 nm. Sufficient Sudan II dye (Sigma, 199656, powder) was added to fully saturate pure acetone at RT. 200 μl of saturated solution was added to each 1.5 mL Eppendorf tubes then allowed to fully evaporate to deposit Sudan II dye to the well surface. This coating significantly exceeds the dissolving capacity of 1 mL of aqueous solution. 5 mL of eFLASH buffer was collected at various time points from multiple independent experiments (N = 6). 1 mL of each sample was added to the dye-coated 1.5 mL tubes then incubated at 60°C for 1 hour and then at RT overnight while shaking. 700 μL from each sample was pipetted into a cuvette and absorbance values were recoded using a spectrophotometer. NaDC concentration was calculated based on a standard curve generated using the method described above from solutions with known concentrations of NaDC (Extended Data Fig. 2e).

SHIELD processing. Preservation of mouse brain hemispheres was carried out according to the previously published SHIELD protocol[12]. Mice were transcardially perfused with ice-cold PBS and then with the SHIELD perfusion solution. Dissected brains or organs were incubated in the same perfusion solution at 4 °C for 48 hours. Tissues were then transferred to the SHIELD-OFF solution (1X PBS containing 10% (w/v) P3PE) and incubated at 4°C for 24 hours. In the case of brain hemisphere processing, a whole brain was split into hemispheres before being incubated in the SHIELD-OFF solution. Following the SHIELD-OFF step, the organs were placed in the SHIELD-ON solution (0.1 M sodium carbonate buffer at pH 10) and incubated at 37°C for 24 hours.

For whole mouse brains and whole rat brains received as already PFA-fixed, they were post-fixed with SHIELD instead. PFA-fixed tissues incubated in SHIELD-OFF solution at 4°C for 4-5 days with one exchange of fresh SHIELD-OFF solution halfway through, afterwards the brains were

incubated in SHIELD-ON solution at RT for 24 hours. Processed samples are washed in PBS for at least 24 hours with multiple solution exchanges.

Marmoset brains perfused with ice-cold PBS and then with SHIELD perfusion solution were incubated in the same perfusion solution at 4°C for 48 hours. The brain was hemisected, transferred to the SHIELD-OFF solution, and incubated at 4°C for 24 hours. Following the SHIELD-OFF step, the hemispheres were incubated in the SHIELD-ON solution at 37°C for 24 hours. Afterwards the hemispheres were transferred to PBS for washing.

Formalin-fixed human tissues were obtained from Massachusetts General Hospital brain tank. The 4-mm-thick coronal slabs were incubated in the SHIELD-OFF solution for 48 hours. Following the SHIELD-OFF step, the tissues are incubated in the SHIELD-ON solution at 37°C.

Organoids were fixed in 1X PBS with 4% (w/v) PFA at RT for 30 minutes and subsequently incubated in SHIELD-OFF solution at 4°C for 48 hours. Samples were then incubated in SHIELD-ON solution at 37°C overnight before washing with PBS with 0.02% sodium azide at RT for at least 24 hours.

Passive clearing (delipidation). SHIELD-processed samples were delipidated before labeling or imaging. Passive delipidation was done by incubating tissues in the clearing buffer (300 mM SDS, 10 mM sodium borate, 100 mM sodium sulfite, pH 9.0). Thin slices between 100 μm and 200 μm thickness were cleared at 45°C clearing buffer for 2-3 hours. Mouse brain hemispheres were cleared at 45°C for 10-14 days. Organoids were cleared at 55°C for 36 hours. Human tissue slab was cleared at 80°C until translucent for approximately one week.

Active clearing (Stochastic Electrotransport). SHIELD-processed samples can also be cleared rapidly using stochastic electrotransport (SmartClear Pro, LifeCanvas Technologies). Mouse brain hemispheres were cleared at 45°C for 3-4 days. Whole mouse brains were cleared for approximately one week. Whole rat brains were cleared for approximately 10 days. The marmoset brain hemisphere was cut coronally into 4 blocks of 8 mm-thickness using a microtome and the blocks were cleared for 2 weeks.

Antibody destaining. Samples previously labeled with antibodies are first incubated in fresh clearing buffer overnight at 37°C. Afterwards the samples are moved to 50 mL of preheated 80°C clearing buffer on heated shaker for 1 hour, maintaining the temperature at 80°C. Afterwards, the samples are transferred to fresh RT clearing buffer and incubated overnighted on shaker at 37°C. The sample was washed using PBS with multiple solution exchanges for one day to thoroughly wash out SDS. Only SHIELD-processed samples are compatible with this destaining protocol.

Passive immunohistochemistry. Immunohistochemistry was performed on 100 μm- or 200 μm-thick mouse or marmoset brain tissue sections. Staining was performed on 24 or 48 well plates with primary antibodies (per recommended dilution from each vendors) and with dye-conjugated Fc-specific Fab secondary antibodies (1:3 molar ratio between Fab fragments and the primary antibody, Jackson Immunoresearch) or dye-conjugated IgG secondary antibodies (1:2 molar ratio between full size secondary antibody and primary antibody, abcam) for 1 day at RT in PBS with 0.1% Triton X-100 (PBST). Similar protocols were used to characterize antibody binding performance in several different buffers: 50 mM Tris buffer with 0.1% NaDC, 50 mM Tris with 1% NaDC, eFLASH initial buffer, and eFLASH terminal buffer (buffer retrieved from the eFLASH staining device after 24 hours).

Immunohistochemistry for pH and NaDC effect characterization. For buffer characterization in Figure 2a-b and Extended Data Figure 3a, initial primary antibody staining of 100 μm mouse tissue sections with anti-PV and anti-NPY in was shortened to 2 hours at 37°C in experimental conditions: 50 mM Tris buffer with pH 7.5, pH 9, pH 10, pH 7.5 with 0.1% NaDC, pH 7.5 with 1% NaDC, and pH 10 with 1% NaDC. After brief washing in their respective buffers for 1 hour then in PBS for 1 hour, samples are labeled with Alexa 647 secondary antibody for 4 hours. After another round of washing for 4 hours, samples are briefly fixed in 4% PFA in PBS for 1 hour at 37°C then thoroughly washed with PBS overnight at RT. Finally, an additional round of normal immunohistochemistry is performed in PBST with additional primary antibodies and Alexa 488 secondary antibodies. Segmentation masks for soma intensity analysis were drawn based on Alexa 488 channel using ImageJ. N = 3 independent experiments for each condition. Total number of cells per condition respectively for anti-PV: 139, 97, 97, 101, 93, and 66. Total number of cells per condition respectively for anti-NPY: 43, 31, 21, 21, 23, and 21.

eFLASH protocol. Volumetric immunolabeling with eFLASH was carried out with a device described in Kim et al.[37] Experiments were carried out with two buffers. The main buffer (100 mM Tris, 4% (w/v) D-sorbitol, 0.1% (v/v) Triton X-100, 0.1% (w/v) NaDC, titrated to pH 9.5 with formic acid) is a circulation solution that allows conduction of electricity. The sample buffer (100 mM Tris, 4% (w/v) D-sorbitol, 0.2% (v/v) Triton X-100, 1% (w/v) NaDC, titrated to pH 9.5 with formic acid) is used to fill the sample cup along with the tissue and antibodies. 350 mL of the main buffer was loaded into the staining device and 2-10 mL of the sample buffer was loaded into the sample cup, adjusted based on the sample to fully submerge the sample. The tissue sample was placed in a nylon mesh then placed into the sample cup to prevent direct contact with the nanoporous membrane of the sample cups. For one-shot labeling, primary antibodies and secondary Fc-specific Fab fragment antibodies were added to the sample cup at the sample time, 1:2 molar ratio. For separate labeling of primary and secondary antibodies (non-Fc-specific Fab fragment antibodies), two rounds of eFLASH labeling are performed back-to-back with washing in between. For secondary antibody labeling only, alternate buffers can be used for shorter 4-6 hours experiments: 100 mM Tris, 0.1% (v/v) Triton X-100, 0.1% (w/v) NaDC, titrated to pH 8 with formic acid for both main chamber (350 mL) and sample cup (2-10 mL). For a single round of eFLASH experiment, electric field is applied for 24 hours at 90 V with maximum current limited to 500 mA. Temperature control was set to maintain 25°C. Sample cup stir bar rotation was set to 850 rpm and sample cup rotation speed was set to 0.01 rpm. Suggested amount of primary antibodies for whole mouse brain-sized samples are included in Supplementary Table 1.

Dye conjugation of secondary antibodies. For the far-red channel, secondary antibodies conjugated with SeTau647 were used for most labeling experiments as they provide superior photo-stability when compared to commercially available dyes[80]. SeTau-647-NHS was purchased from SETA BioMedicals and 10 μl 10 mM aliquots were prepared using DMSO (anhydrous, ZerO2®, ≥99.9%, Sigma). SeTau-647-NHS were reacted with non-conjugated Fc-specific Fab fragments at 10:1 ratio (Jackson Immunoresearch) for 1 hour at RT. Afterwards, the solution was purified using Zeba Spin Desalting Columns (7k MWCO, ThermoFisher Scientific) 2 to 3 times until the desalting column ran clean. The concentration of the resulting solution was measured using DC™ Protein Assay (Bio-Rad) before use.

Refractive index matching. Optical clearing of delipidated samples was achieved using Protos-based immersion medium[12]. For samples thicker than 1 mm, optical clearing was done in two steps. Labeled samples were first incubated in half-step solution (50/50 mix of 2X PBS and Protos-based immersion medium) at 37°C overnight. Afterwards, the samples were moved to the pure immersion medium and incubated at 37°C overnight.

Fixation of labeled samples. For antibodies that are not stable in Protos-based immersion medium, the eFLASH-labeled samples were fixed with 4% (w/v) PFA to prevent dissociation of bound antibodies. eFLASH-labeled samples were first washed in 1X PBS with 0.02% (w/v) sodium azide at RT for at least 6 hours to wash out Tris. Samples were then moved to freshly prepared 4% (w/v) PFA solution in 1X PBS and placed on an orbital shaker at RT overnight. Samples were then washed with 1X PBS with 0.02% (w/v) sodium azide at RT with multiple solution exchanges for at least 6 hours.

Light-sheet imaging and post-processing. Rapid volumetric imaging was performed with an axially swept light-sheet microscope (SmartSPIM, Lifecanvas Technologies, MA) equipped with three lasers (488 nm, 561 nm, 642 nm). The microscope focus was fine-tuned for each sample by finely adjusting the position of the illumination objectives to ensure optimal optical sectioning. Focus compensation was programmed as a function of depth for each laser line to account for slight focal variations through imaging depth. All light-sheet imaging was done with either the 3.6x objective (custom Lifecanvas design, 0.2NA 12 mm WD lateral resolution 1.8 μm in XY) and the 10x objective (Olympus XLPLN10XSVMP, 0.6NA, 8 mm WD, lateral resolution 0.66 μm in XY). Acquired data was post-processed with algorithms described in Swaney et al.[63]. A complete table of imaging modalities and conditions for every data included in this paper can be found in Supplementary table 2. For visualization Imaris (Bitplane, Switzerland) and ImageJ were used.

Volumetric cell detection. Detection of cells is accomplished by blob detection, followed by dimensionality reduction and classification. Blobs are detected by computing the difference of Gaussians followed by identification of voxels that are the maximum of their neighbors within a chosen radius. 31x31 pixel patches are then extracted in the X/Y, X/Z and Y/Z planes. The raster of these patches is concatenated, and the three resulting 961-element vectors are concatenated to create a 2883-feature vector. All patches of putative cell centers within the volume are collected

and PCA is performed to reduce the dimensionality of the vector to 48 components. Each of these components are composed of 2883 elements which are multiplied with the 2883-feature vector per patch to produce 48 numerical features. The vector of each component can be visualized as three 31x31 planes to allow interpretation of the magnitude of the component. The 48 numerical features are then used to train a random forest classifier using iterative user-supervised training. Finally, the classifier is applied to all patches in the volume to classify each local maximum as a positive cell detection or negative artifact detection.

Atlas alignment. Atlas alignments of mouse brain hemispheres labeled with eFLASH to the Allen brain reference atlas, CCF V3[81], were carried out using the hybrid automated atlas alignment method described in Swaney et al[63], which combines Elastix[82] and manual refinement tools to improve alignment accuracy.

Brain region segmentation. Detected cell coordinates were transformed from the original coordinate space to the reference coordinate after atlas alignment. The alignment was used to construct a three-dimensional radial basis function using thin-plate spines to map points in the original coordinate space to the reference coordinate space. The point locations in the reference space were then matched against the Allen Brain Mouse Atlas[81] reference segmentation to yield counts per brain region. These counts were then used to color the regions in the Allen Brain Mouse Atlas coronal SVG image files. Calculations and visualizations were done using the Nuggt python package[63].

Code availability. The custom code used in this study is available from the corresponding author upon reasonable request.

Data availability. The data supporting the findings of this study are available from the corresponding author upon reasonable request.

Figure 1. Conceptual description and computational modeling of CuRVE. (**a**) Schematic description comparing conventional chemical processing of ultrathin tissues and intact tissues. Ultrathin tissues experience near instant dispersion of chemical environment, allowing equal processing of all cells. Intact organs experience slow volumetric dispersion leading to disruption of spatial equilibrium and thus disparate cellular processing. (**b**) Schematic description of CuRVE for equal volumetric processing. Chemical environments are shifted gradually and allowed to re-establish equilibrium before proceeding with the subsequent gradual shift. With the continuous maintenance of spatial equilibrium, all cells can experience equal processing through the volume. (**c-g**) Computational modeling of CuRVE in COMSOL for volumetric immunolabeling. Model for conventional constant reaction methodology, static binding strength (left, blue line). Model for CuRVE, swept binding strength (right, red line). (**c**) Normalized reaction strength modulation through time. (**d**) Concentration of unbound antibodies evaluated near the surface (dotted line) and the center (solid line) throughout the simulation duration. Purple vertical dotted lines indicate the time point where 99% of the antibody-antigen complexes are formed relative to the T =1. Static, SE only (left), Swept, CuRVE + SE (right). (**e**) Concentration of antibody-antigen complexes throughout the volume represented by a color heatmap. Time points shown are relative to the 99% bound time point indicated in **d**. T = 0, 0.09, 0.18 for SE only. T = 0, 0.3, 0.6 for CuRVE + SE. (**f**) Overlaid concentration profiles of antibody-antigen complexes through the center of the volume at the end of the simulation. Volume rendering of the SE only model (left), and the CuRVE + SE model (right). (**g**) Sensitivity analysis via parametric sweep of antigen density, forward reaction rate, antibody to antigen ratio, and tissue thickness. The uniformity index represents the flatness of the concentration profile given by concentration at center divided by maximum concentration at T = 1. Data points evaluated with matching parameters are linked via dotted lines.

Figure 2. Design and validation of eFLASH system. (**a**) Effect of pH and sodium deoxycholate (NaDC) concentration on binding of anti-NPY and anti-PV antibodies. Normalized average soma fluorescence intensities (N = 3 independent experiments for each condition, each soma shown as an individual data point). One-Way ANOVA multiple comparisons, *P < 0.05, ***P < 0.001, ****P < 0.0001. Mean ± s.d.. (**b**) Representative images for data in **a** shown in two different display ranges. 0/4095 (top row). 0/1500 (bottom row). Scale bar = 20 μm (white). (**c**) Schematic of the eFLASH system. The pH and NaDC concentration of the labeling solution are gradually reduced to sweep the molecular probes' binding affinity from low to normal binding strength in the context of stochastic electrotransport (SE). Electrocatalytic oxidation of d-sorbitol on the anode surface generates acidic components that lower pH. NaDC concentration of the labeling solution is reduced by the diffusion of NaDC monomers through the nanoporous membrane. (**d**) Measurement of pH (N = 4 independent experiments) and NaDC concentration (N = 6 independent experiments) throughout the 24-hour processing. Mean ± s.e.m.. (**e-f**) Volumetric labeling of two hemispheres of a single brain with SE and eFLASH respectively using the same mass of antibodies: 3 μg of anti-CB (Calbindin) and 5 μg of anti-NF (Neurofilament marker). Optical plane of three-dimensional (3D) volumetric data. 20 μm max intensity projections (MIP).

Sagittal (original imaging plane) and coronal (reconstructed plane). Distance of the sagittal optical plane from the medial plane (**e**) z = 2.8 mm, (**f**) z = 3.1 mm. Zoomed in view of the coronal layers (**e-i, f-i**), striatum (**e-ii, f-ii**), and cerebellum (**e-iii, f-iii**). Scale bars = 2 mm (cyan), 100 μm (white).

Figure 3. Rapid, uniform, and universal volumetric immunolabeling using eFLASH. (**a**) Whole volume rendering, representative optical section, and magnified images (**a-i-iv**) of whole rat brain labeled with anti-NeuN. Supplementary Video 3. (**b**) Representative optical section and magnified images (**b-i-iii**) of whole mouse brain labeled with anti-PV. Supplementary Video 4. (**c**) Representative optical section and magnified images (**c-i-iii**) of mouse brain hemisphere simultaneously labeled with anti-NeuN, anti-TH, and anti-ChAT antibodies. Supplementary Video 5. (**d-e**) Whole volume rending, representative optical section (170 μm MIP), and magnified images (**d-i-ii, e-i-ii**) of marmoset brain block containing visual cortex (5 mm x 5 mm x 8 mm) labeled with (**d**) round 1: anti-PV and (**e**) round 2: anti-NPY (round 2). Supplementary Video 6. (**f**) Whole volume rendering, representative optical section, and magnified images (**f-i-ii**) of mouse embryo labeled with anti-mouse Ret and anti-NF-M. Optical sections are 20 μm MIP unless specified otherwise. Scale bars = 2 mm (cyan), 200 μm (white).

Figure 4. Holistic comparison of transgenic and immunolabeling-based cell-type labeling. (**a-c**) 3D dataset from a PV-Cre and *loxP*-tdTomato dual transgenic mouse hemisphere stained with anti-PV antibody. (**a**) Representative optical section. (**b**) Magnified images of **a**. (**c**) A percentage plot for tdTomato-only (red), anti-PV-only (green), and tdTomato and anti-PV co-positive cells (yellow) among all the labeled cells in individual representative brain regions. (**d-h**) 3D dataset of a $ChAT^{BAC}$-eGFP mouse brain stained with anti-ChAT antibody. (**d**) Whole volume rendering. (**e**) Magnified images of **d**. (**f**) A percentage plot for EGFP-only (green), anti-ChAT-only (red), and EGFP and anti-ChAT co-positive cells (yellow) among all the labeled cells in individual representative brain regions. (**g**) Magnified view of **d**. (**h**) Zoom-in view of **g**. Scale bars = 2 mm (cyan), 200 μm (white). M1, primary motor cortex; S1, primary somatosensory cortex; A1, primary auditory cortex; V1, primary visual cortex; RSA, retrosplenial cortex; PPA, posterior parietal association cortex; AC, anterior cingulate cortex; Piri, piriform cortex; Ecto, ectorhinal cortex; lEnto, lateral entorhinal cortex; CPu, caudoputamen; NAc, nucleus accumbens; CeA, central amygdala; BLAa, basolateral amygdala, anterior part; BLAp, basolateral amygdala, posterior part; LA, lateral amygdala; DG, dentate gyrus; mo, dentate gyrus, molecular layer; sg, dentate gyrus, granule cell layer; po, dentate gyrus, polymorph layer; CA1, hippocampal CA1; CA3, hippocampal CA3; 5N, motor nucleus of trigeminal; dNAmb, nucleus ambiguus, dorsal part; vNAmb, nucleus ambiguus, ventral part.

Figure 5. Significant individual variability of anti-PV+ expression in wildtype and PV-Cre/*loxP*-tdTomato mice. (**a**) High-resolution imaging of LPZ (**a-i**) and normal region (**a-ii**), labeled with anti-PV, anti-Gephyrin, and anti-NeuN in wildtype mouse. (**b**) Additional round of immunolabeling of eFLASH-labeled tissue (with rabbit host anti-PV, green) using mouse-host PV antibody (red). White arrows indicate PV-Cre/*loxP*-tdTomato expression (blue) that is disparate from both antibody labeling. (**c**) Representative optical section of wildtype mice labeled with anti-

PV (cyan) and anti-CB (magenta) and representative regions with LPZ. (**c-i-ii**) with zoomed in images. (**c-i**) Seven PV-cre and *loxP*-tdTomato double-transgenic mouse brains were eFLASH labeled with anti-PV antibody. (**d**) Representative optical section of PV-Cre/*loxP*-tdTomato (magenta) mice labeled with anti-PV (cyan) and representative regions with LPZ. (**d-i-ii**) with zoomed in images. (**e**) 3D segmentation of low PV soma density regions in the seven brains. Brains 1-3 are littermates. (**f**) Total volumes of low PV regions in individual brains. (**g**) Quantification of the low PV region volumes in each brain area in the left and right hemispheres. Brain-wide quantification of PV+ cells identified based on (**h**) protein expression and (**i**) genetic fluorescent protein expression. Bottom row bar graph represents coefficient of variance for the regional densities between the seven brains. Scale bars, 2 mm (cyan), 100 μm (white), and 20 μm (yellow). 20 μm MIP optical sections. FRP, frontal pole of the cerebral cortex; MO, somatomotor areas; SS, somatosensory areas; GU, gustatory areas; VISC, visceral area; AUD, auditory areas; VIS, visual areas; ACA, anterior cingulate area; PL, prelimbic area; IL, infralimbic area; ORB, orbital area; AI, agranular insular area; RSP, retrosplenial area; PTLp, posterior parietal association area; TEa, temporal association areas; ECT, ectorhinal araea; ENT, entorhinal area; Str, striatum; CPu, caudoputamen; NAc, nucleus accumbens; PostS, postsubiculum; PreS, presubiculum; DG, dentate gyrus; CA1, hippocampal CA1; CA2, hippocampal CA2; CA3, hippocampal CA3.

Extended Data Figure 1. Extended computational modeling of CuRVE. (**a-c**) Computational modeling of CuRVE in COMSOL for volumetric immunolabeling with simple diffusion. Model for conventional constant reaction methodology, static binding strength (left, blue line). Model for CuRVE, swept binding strength (right, red line). (**a**) Normalized reaction strength modulation through time. Note that the experimental duration is normalized to simulations on Figure 1**c-g**, which share identical parameters except the reaction rate and effective diffusivity. (**b**) Concentration of unbound antibodies evaluated near the surface (dotted line) and the center (solid line) throughout the simulation duration. Static, simple diffusion (left), Swept, CuRVE (right). (**c**) Concentration of antibody-antigen complexes throughout the volume represented by a color heatmap. Time points rendered: T=0, 16.5, 33 for both simulations. (**d**) Overlaid concentration profiles of antibody-antigen complexes through the center of the volume at the end of the simulation. Volume rendering of the simple diffusion model (left), and the CuRVE model (right). (**e-g**) Sensitivity analysis of CuRVE, SWITCH, and constant reaction scenarios. (**e**) The uniformity index represents the flatness of the Ag-Ab complex concentration profile given by concentration at center divided by maximum concentration. (**f**) Normalized reaction strength profile throughout the experiment: CuRVE (red), SWITCH (black), constant reaction (reduced rate) (green), and constant reaction (blue). (**g**) Sensitivity analysis through parametric sweep of four different variables. Tissue antigen density variability: 4.74e-10, 1.5e-9, 4.74e-9, 1.5e-8, 4.74e-8, 1.5e-7 [mol/L]. Equilibrium dissociation constant variability (i.e., antibody kinetic properties): 1e-7, 1e-8, 1e-9, 1e-10, 1e-11, 1e-12 [mol/L]. Antibody titration variability (i.e., antibody to antigen molar ratio): 0.1, 0.3, 0.5, 0.7, 0.9, 1.1. Tissue thickness variability: 5, 10, 15, 20, 25, 30 [mm]. CuRVE + SE (red circle). SWITCH + SE (grey circle). Partial inhibition + SE (green circle). SE only (blue circle). Data points evaluated with matching parameters are linked via dotted lines.

Extended Data Figure 2. Validation of antibody binding modulation for volumetric immunolabeling. (**a**) Representative microscopy images and segmentation masks generated for quantification of the effect of pH and NaDC concentration on antibody binding. Initial labeling conducted in respective buffers with Alexa 647 secondary (green) and additional labeling conducted with additional primary antibody and Alexa 488 secondary (red) for getting accurate soma masks. (**b-c**) Representative images and quantification of antibody displacement under electrophoresis in buffer containing 0% (green), 0.1% (blue), and 1% (red) NaDC respectively. Solid lines show the average normalized fluorescent intensities along the gel length. Individual data shown in lighter dotted lines. (**c**) Relative effective diffusivity of data in **b** calculated and normalized to 0% NaDC based on centroid of area under the curve. *N* = 3 independent experiments. One-Way ANOVA multiple comparisons, **P < 0.005. Mean and individual data shown. (**d**) Representative images of 24 antibodies labeled in PBST, initial state of eFLASH buffer (i.e., antibody binding inhibitive state), and terminal state of eFLASH buffer (i.e., nominal state). Scale bar = 100 μm (white). (**e**) Calibration curve for spectrographic absorption of Sudan II dye at 592 nm for measuring NaDC concentration.

Extended Data Figure 3. Volumetric immunolabeling of various mammalian organs and organoids using eFLASH. (**a-g**) Whole volume rendering and representative optical plane image followed by magnified images. (**a**) Human iPS-derived cerebral organoid immunolabeled with anti-Vimentin (green), anti-β-tubulin (red), and SYTO 16. (**a-i-ii**) Magnified images of neuroepithelial formation around putative ventricles. (**b**) Human brain block containing grey and white matter regions immunolabeled with anti-NPY (white). (**b-i-ii**) Magnified images deep inside the white matter region. (**c**) Mouse liver lobule immunolabeled with anti-Histone-H3 (white). (**c-i-ii**) magnified images near the surface and the center regions. (**d**) Intestine section of $ChAT^{BAC}$-eGFP (green) transgenic mouse immunolabeled anti-β-tubulin (red). (**d-i-ii**) Magnified images of the villi structures. (**e**) Mouse lung immunolabeled with anti-α-SMA (red) and SYTO16. (**e-i-ii**) Magnified images of the airways accompanied by pulmonary and intraacinar arteries. (**f**) Ear canal of Thy1-EGFP (green) transgenic mouse immunolabeled with anti-Myosin VIIa (red) (**f-i-ii**) Magnified images of stereocilia and surrounding actin-based motor structures. (**g**) Mouse heart immunolabeled with anti-TH (green) and anti-α-SMA (red). (**g-i-ii**) Magnified images of dopaminergic innervations and actin filaments. Scale bars = 2 mm (cyan), 100 μm (white).

Extended Data Figure 4. Volumetric immunolabeling of mouse brains with various cell-type markers using eFLASH. (**a-q**) Representative optical plane from 3D imaging data (top), 20 μm MIP (middle), and (**i-iii**) magnified images (bottom): (**a**) anti-neuropeptide Y (NPY), neuronal marker, (**b**) anti-calbindin (CB), neuronal marker, (**c**) anti-choline acetyltransferase (ChAT), cholinergic neuronal marker, (**d**) anti-neurofilament-M (NF-M), neuronal structural marker, (**e**) anti-neuronal nuclei (NeuN), pan-neuronal marker, (**f**) anti-tyrosine hydroxylase (TH), dopaminergic neuronal marker, (**g**) anti-vasoactive intestinal peptide (VIP), neuroendocrine marker, (**h**) anti-somatostatin (SST), GABAergic interneuron marker, (**i**) anti-neuronal nitric oxide synthases (nNOS), GABAergic interneuron marker, (**j**) anti-ionized calcium binding adaptor

molecule (iba1), microglial and macrophage marker, (**k**) anti-glial fibrillary acidic protein (GFAP), astrocyte and neural stem cell marker (**l**) anti-tryptophan hydroxylase 2 (TPH2), serotonergic neuronal marker, (**m**) tomato lectin, vasculature stain, (**n**) anti-c-FOS, neuronal activity marker, (**o**) anti-neurofilament marker SMI-312 (anti-NF), pan-axonal marker, (**p**) anti-calretinin (CR), and (**q**) SYTO 16, nucleic acid stain. Scale bars = 1 mm (cyan), 100 μm (white).

Extended Data Figure 5. Quantitative brain-wide cell type mapping. (**a**) Representative optical section images of intact mouse hemispheres immunolabeled using eFLASH. Automatically detected cell center coordinates are overlayed as red dots. (**b**) Magnified images of **a**. (**c**) Representative coronal plane heatmaps of 3D cell type density data. (**d**) Representative optical section image of dual immunolabeling using eFLASH. Anti-NPY (yellow) and anti-SST (magenta) co-positive cell center coordinates are overlayed with red dots. (**e**) Magnified images of **d**. (**f**) Representative coronal plane heatmaps of the 3D NPY/SST co-positivity data. (**g**) Representative optical section image of anti-c-Fos immunolabeling using eFLASH. The mouse experienced contextual fear conditioning 90 minutes before sacrifice. (**h**) Magnified images of **g**. (**i**) Representative coronal plane heatmaps of the c-Fos+ cell density data. Scale bars = 2 mm (cyan) and 20 μm (white).

Extended Data Figure 6. Large-scale regionalized loss of anti-PV+ cells in prefrontal cortex of adult wildtype mice. (**a**) Adult (P56) male whole mouse brains labeled with anti-PV (cyan) and anti-CB or anti-nNOS (magenta) using eFLASH. Observed with low-PV zones (LPZs). Representative optical sections (horizontal plane) and magnified images of regions marked with dotted boxes. 20 μm MIP. Mice bred at MIT facility. (**b-c**) Randomly chosen 11 mouse brains sourced from (**b**) UCSD and (**c**) Hilltop Lab Animals (Scottdale, PA). 200 μm-thick horizontal mouse brain sections passively immunolabeled with anti-PV (cyan) and DAPI (magenta). (**b**) 20-40 μm MIP images from 6 adult (8 weeks old) male mice samples. (**c**) 20-40 μm MIP images from 5 adult (10 weeks old) female mice samples. Dotted box regions are chosen to highlight low anti-PV cell density regions if present. Scale bars = 2 mm (cyan) and 200 μm (white)

Extended Data Figure 7. Validation of low PV soma density regions. (**a-c**) Quantification of gephyrin clusters in low PV (red bars) and normal regions (green bars). (**a**) Density of Gephyrin clusters. (**b-c**) Fraction of gephyrin clusters co-positive with anti-PV, averaged in each ROI (**b**) and in each brain section (**c**). *N* = 5 animals. 3 ROIs each for low PV and normal regions per animal. One-Way ANOVA, n.s. = not significant, **P < 0.005. (**d-e**) Double passive immunolabeling of PV-Cre/*loxP*-tdTomato (green) mouse horizontal section with rabbit-host anti-PV (red) and mouse-host anti-PV (blue). (**e**) Magnified images from the marked box in **d**. In the inset, MsPV+/RbPV+/tdTomato- cell (white arrow) and MsPV-/RbPV-/tdTomato+ cell (cyan arrow). (**f-g**) Horizontal brain sections from PV-Cre/*loxP*-tdTomato (red) double transgenic mice eFLASH-immunolabeled with anti-PV (green) with additional round of passive labeling: (**f**) anti-NeuN (blue) and (**g**) SYTO16 (blue). (**h**) Passive immunolabeling of anti-PV (red), anti-CB (cyan), and anti-SST (green). Low PV region delineated with dotted white boundary. Scale bars = 2 mm (cyan) and 100 μm (white).

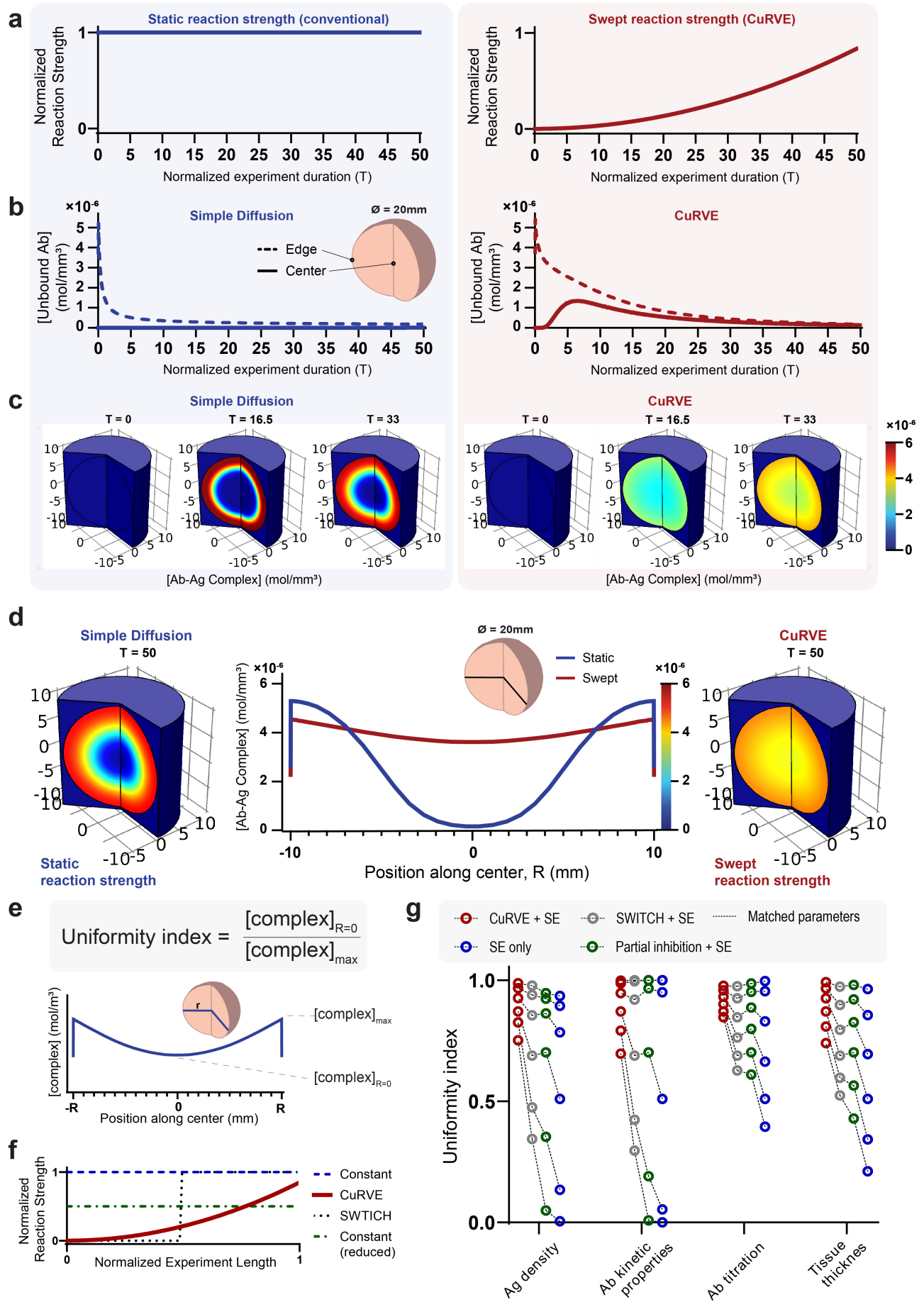

Extended Data Figure 1. Extended computational modeling of CuRVE. (**a-c**) Computational modeling of CuRVE in COMSOL for volumetric immunolabeling with simple diffusion. Model for conventional constant reaction methodology, static binding strength (left, blue line). Model for CuRVE, swept binding strength (right, red line). (**a**) Normalized reaction strength modulation through time. Note that the experimental duration is normalized to simulations on Figure **1c-g**, which share identical parameters except the reaction rate and effective diffusivity. (**b**) Concentration of unbound antibodies evaluated near the surface (dotted line) and the center (solid line) throughout the simulation duration. Static, simple diffusion (left), Swept, CuRVE (right). (**c**) Concentration of antibody-antigen complexes throughout the volume represented by a color heatmap. Time points rendered: T = 0, 16.5, 33 for both simulations. (**d**) Overlaid concentration profiles of antibody-antigen complexes through the center of the volume at the end of the simulation. Volume rendering of the simple diffusion model (left), and the CuRVE model (right). (**e-g**) Sensitivity analysis of CuRVE, SWITCH and constant reaction scenarios. (**e**) The uniformity index represents the flatness of the Ag-Ab complex concentration profile given by concentration at center divided by maximum concentration. (**f**) Normalized reaction strength profile throughout the experiment: CuRVE (red), SWITCH (black), constant reaction (reduced rate) (green), and constant reaction (blue). (**g**) Sensitivity analysis through parametric sweep of four different variables. Tissue antigen density variability: 4.74e-10, 1.5e-9, 4.74e-9, 1.5e-8, 4.74e-8, 1.5e-7 [mol/L]. Equilibrium dissociation constant variability (i.e., antibody kinetic properties): 1e-7, 1e-8, 1e-9, 1e-10, 1e-11, 1e-12 [mol/L]. Antibody titration variability (i.e., antibody to antigen molar ratio): 0.1, 0.3, 0.5, 0.7, 0.9, 1.1. Tissue thickness variability: 5, 10, 15, 20, 25, 30 [mm]. CuRVE + SE (red circle). SWITCH + SE (grey circle). Partial inhibition + SE (green circle). SE only (blue circle). Data points evaluated with matching parameters are linked via dotted lines.

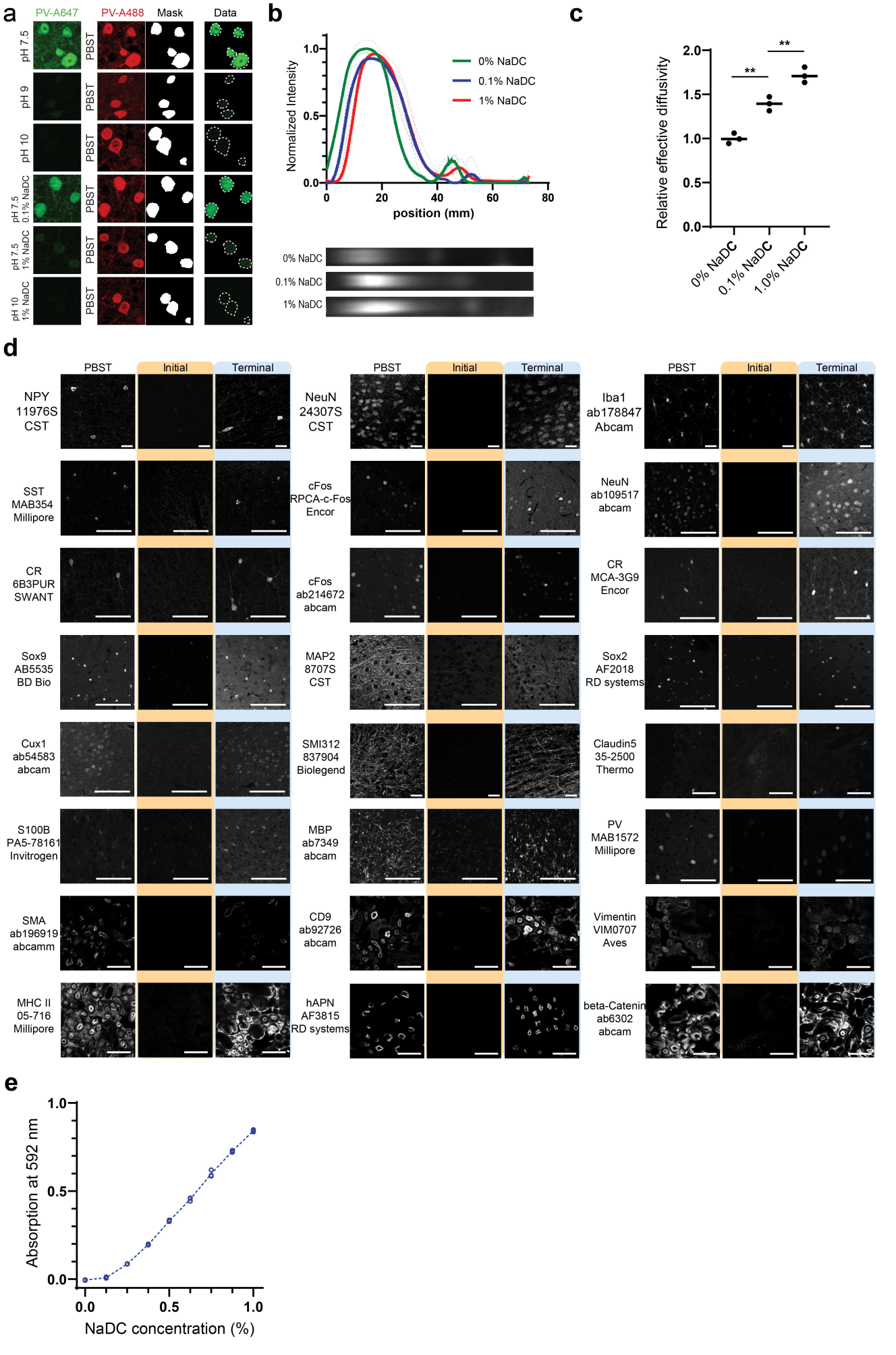

Extended Data Figure 2. Validation of antibody binding modulation for volumetric immunolabeling. (**a**) Representative microscopy images and segmentation masks generated for quantification of the effect of pH and NaDC concentration on antibody binding. Initial labeling conducted in respective buffers with Alexa 647 secondary (green) and additional labeling conducted with additional primary antibody and Alexa 488 secondary (red) for getting accurate soma masks. (**b-c**) Representative images and quantification of antibody displacement under electrophoresis in buffer containing 0% (green), 0.1% (blue), and 1% (red) NaDC respectively. Solid lines show the average normalized fluorescent intensities along the gel length. Individual data shown in lighter dotted lines. (**c**) Relative effective diffusivity of data in **b** calculated and normalized to 0% NaDC based on centroid of area under the curve. N = 3 independent experiments. One-Way ANOVA multiple comparisons, **P < 0.005. Mean and individual data shown. (**d**) Representative images of 24 antibodies labeled in PBST, initial state of eFLASH buffer (i.e., antibody binding inhibitive state), and terminal state of eFLASH buffer (i.e., nominal state). Scale bar = 100 μm (white). (**e**) Calibration curve for spectrographic absorption of Sudan II dye at 592 nm for measuring NaDC concentration.

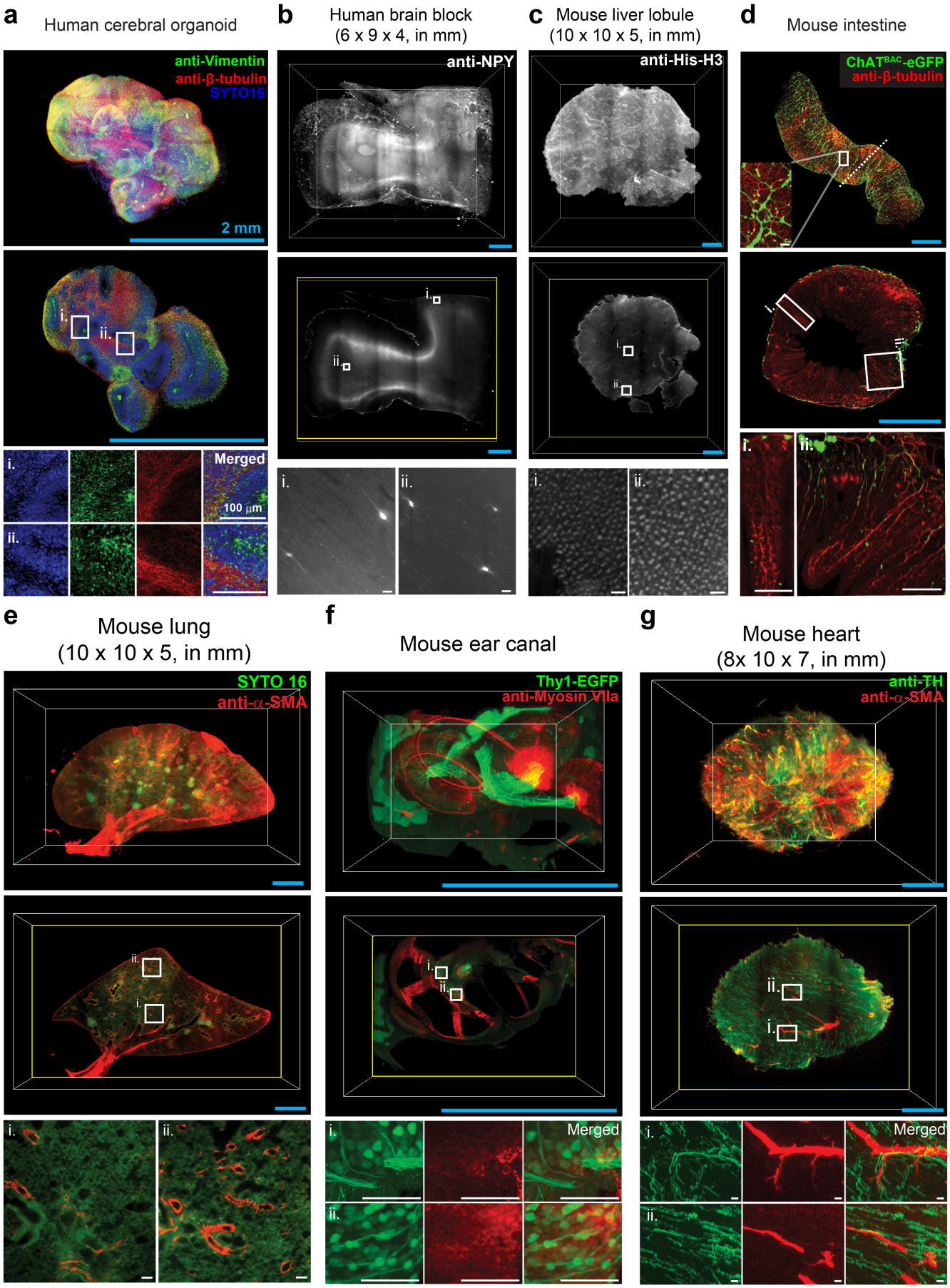

Extended Data Figure 3. Volumetric immunolabeling of various mammalian organs and organoids using eFLASH. (**a-g**) Whole volume rendering and representative optical plane image followed by magnified images. (**a**) Human iPS-derived cerebral organoid immunolabeled with anti-Vimentin (green), anti-β-tubulin (red), and SYTO 16. (**a-i-ii**) Magnified images of neuroepithelial formation around putative ventricles. (**b**) Human brain block containing grey and white matter regions immunolabeled with anti-NPY (white). (**b-i-ii**) Magnified images deep inside the white matter region. (**c**) Mouse liver lobule immunolabeled with anti-Histone-H3 (white). (**c-i-ii**) magnified images near the surface and the center regions. (**d**) Intestine section of ChAT^{BAC}-eGFP (green) transgenic mouse immunolabeled anti-β-tubulin (red). (**d-i-ii**) Magnified images of the villi structures. (**e**) Mouse lung immunolabeled with anti-α-SMA (red) and SYTO16. (**e-i-ii**) Magnified images of the airways accompanied by pulmonary and intraacinar arteries. (**f**) Ear canal of Thy1-EGFP (green) transgenic mouse immunolabeled with anti-Myosin VIIa (red) (**f-i-ii**) Magnified images of stereocilia and surrounding actin-based motor structures. (**g**) Mouse heart immunolabeled with anti-TH (green) and anti-α-SMA (red). (**g-i-ii**) Magnified images of dopaminergic innervations and actin filaments. Scale bars = 2 mm (cyan), 100 μm (white).

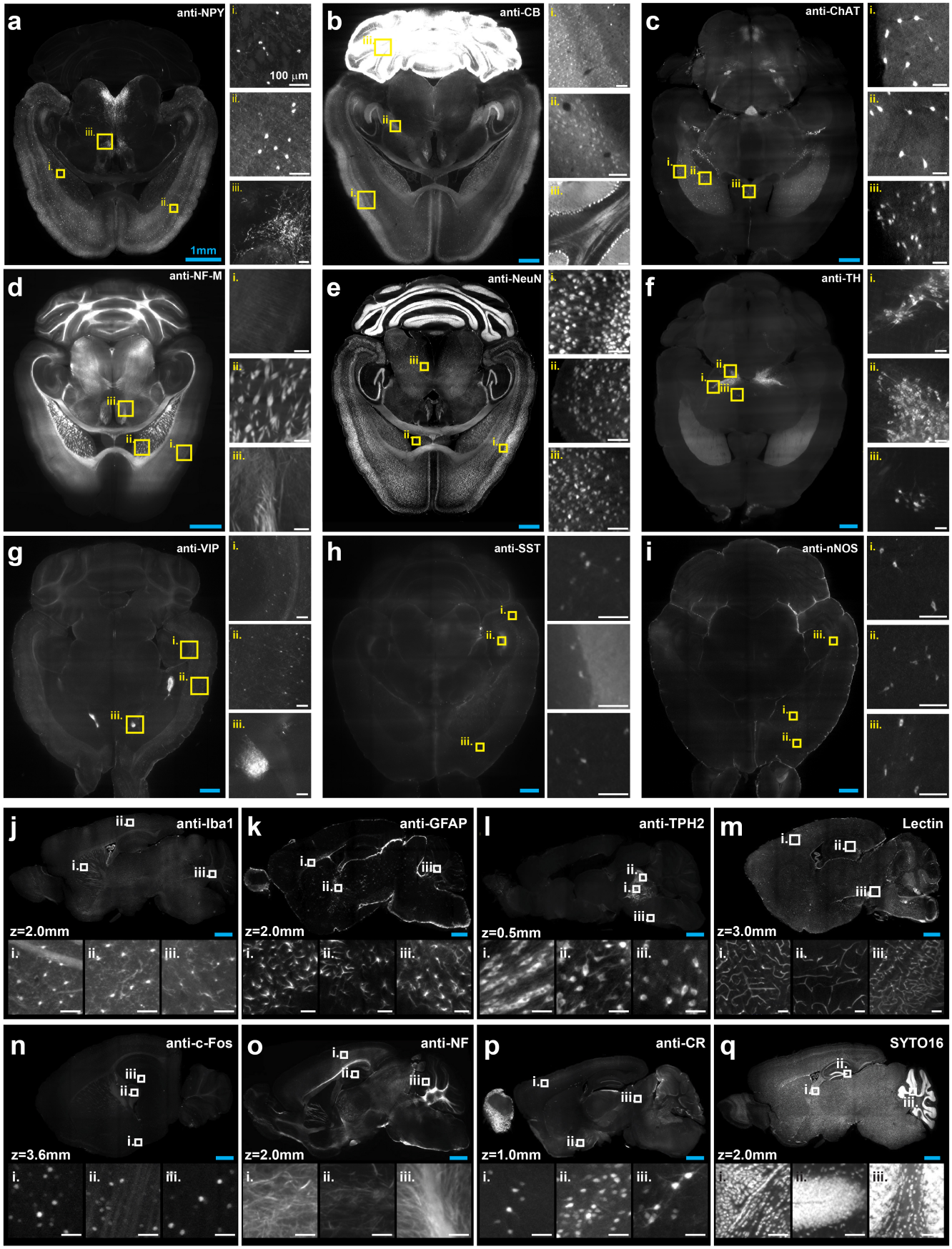

Extended Data Figure 4. Volumetric immunolabeling of mouse brains with various cell-type markers using eFLASH. (**a-q**) Representative optical plane from 3D imaging data (top), 20 μm MIP (middle), and (**i-iii**) magnified images (bottom): (**a**) anti-neuropeptide Y (NPY), neuronal marker, (**b**) anti-calbindin (CB), neuronal marker, (**c**) anti-choline acetyltransferase (ChAT), cholinergic neuronal marker, (**d**) anti-neurofilament-M (NF-M), neuronal structural marker, (**e**) anti-neuronal nuclei (NeuN), pan-neuronal marker, (**f**) anti-tyrosine hydroxylase (TH), dopaminergic neuronal marker, (**g**) anti-vasoactive intestinal peptide (VIP), neuroendocrine marker, (**h**) anti-somatostatin (SST), GABAergic interneuron marker, (**i**) anti-neuronal nitric oxide synthases (nNOS), GABAergic interneuron marker, (**j**) anti-ionized calcium binding adaptor molecule (iba1), microglial and macrophage marker, (**k**) anti-glial fibrillary acidic protein (GFAP), astrocyte and neural stem cell marker (**l**) anti-tryptophan hydroxylase 2 (TPH2), serotonergic neuronal marker, (**m**) tomato lectin, vasculature stain, (**n**) anti-c-FOS, neuronal activity marker, (**o**) anti-neurofilament marker SMI-312 (anti-NF), pan-axonal marker, (**p**) anti-calretinin (CR), and (**q**) SYTO 16, nucleic acid stain. Scale bars = 1 mm (cyan), 100 μm (white).

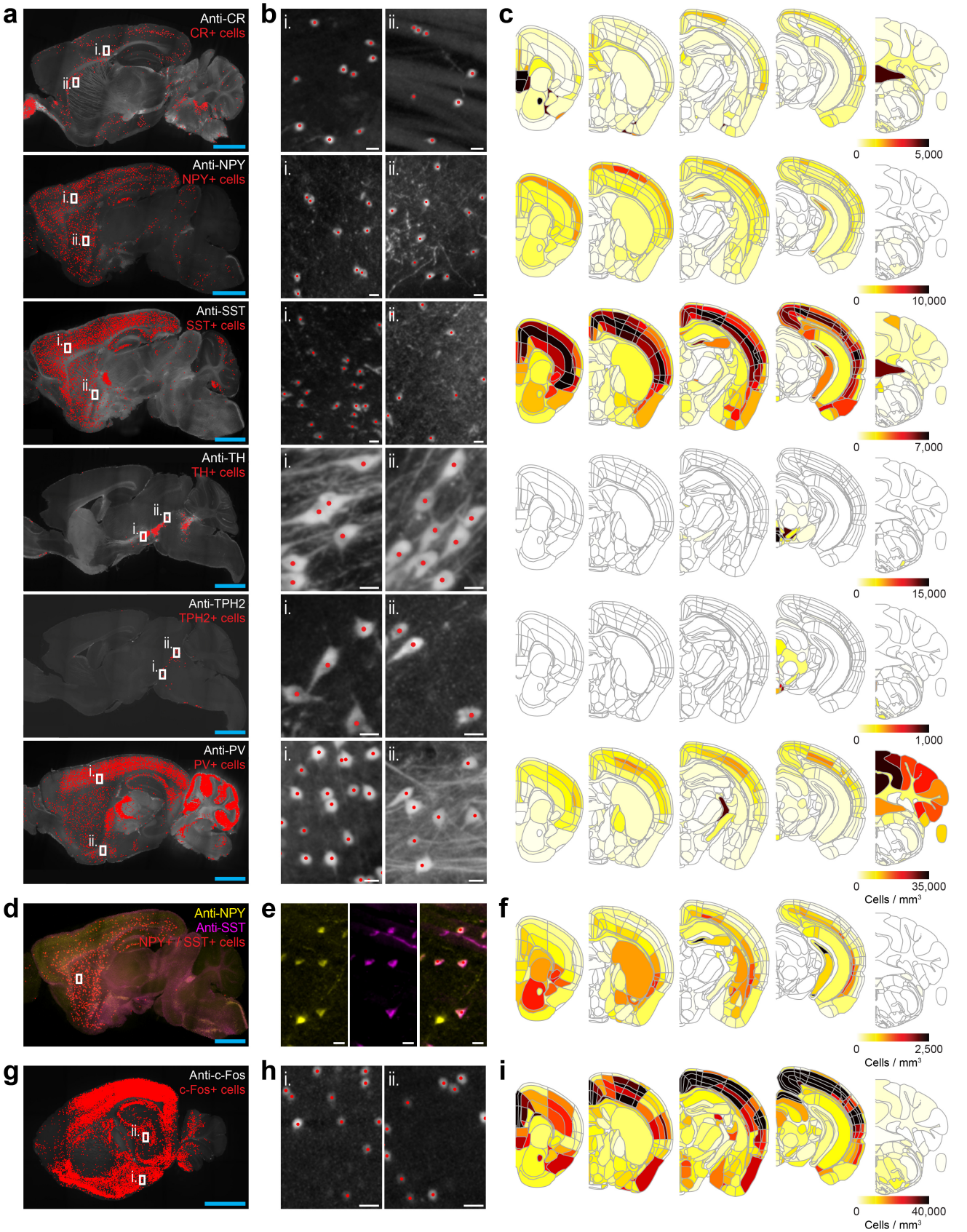

Extended Data Figure 5. Quantitative brain-wide cell type mapping. (**a**) Representative optical section images of intact mouse hemispheres immunolabeled using eFLASH. Automatically detected cell center coordinates are overlayed as red dots. (**b**) Magnified images of **a**. (**c**) Representative coronal plane heatmaps of 3D cell type density data. (**d**) Representative optical section image of dual immunolabeling using eFLASH. Anti-NPY (yellow) and anti-SST (magenta) co-positive cell center coordinates are overlayed with red dots. (**e**) Magnified images of **d**. (**f**) Representative coronal plane heatmaps of the 3D NPY/SST co-positivity data. (**g**) Representative optical section image of anti-c-Fos immunolabeling using eFLASH. The mouse experienced contextual fear conditioning 90 minutes before sacrifice. (**h**) Magnified images of **g**. (**i**) Representative coronal plane heatmaps of the c-Fos+ cell density data. Scale bars = 2 mm (cyan) and 20 μm (white).

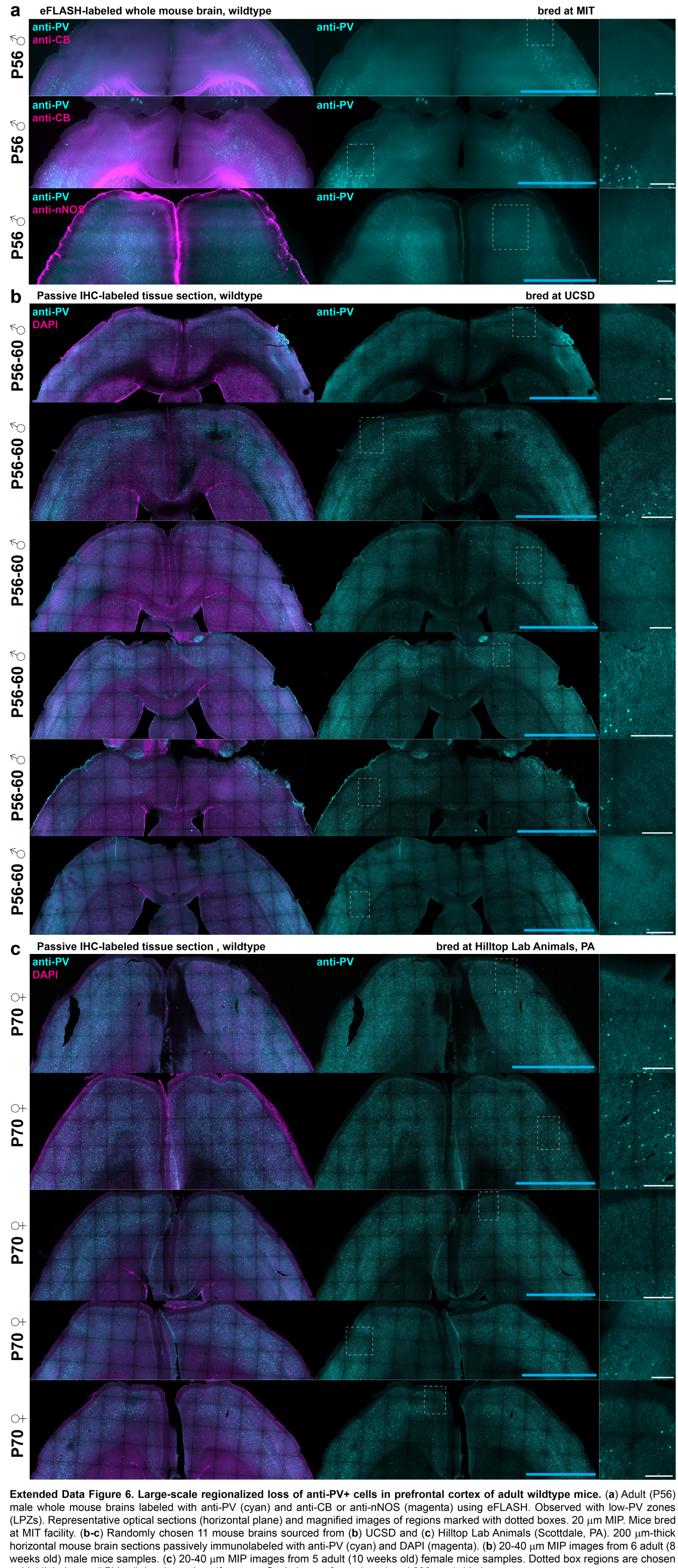

Extended Data Figure 6. Large-scale regionalized loss of anti-PV+ cells in prefrontal cortex of adult wildtype mice. (**a**) Adult (P56) male whole mouse brains labeled with anti-PV (cyan) and anti-CB or anti-nNOS (magenta) using eFLASH. Observed with low-PV zones (LPZs). Representative optical sections (horizontal plane) and magnified images of regions marked with dotted boxes. 20 μm MIP. Mice bred at MIT facility. (**b-c**) Randomly chosen 11 mouse brains sourced from (**b**) UCSD and (**c**) Hilltop Lab Animals (Scottdale, PA). 200 μm-thick horizontal mouse brain sections passively immunolabeled with anti-PV (cyan) and DAPI (magenta). (**b**) 20-40 μm MIP images from 6 adult (8 weeks old) male mice samples. (**c**) 20-40 μm MIP images from 5 adult (10 weeks old) female mice samples. Dotted box regions are chosen to highlight low anti-PV cell density regions if present. Scale bars = 2 mm (cyan) and 200 μm (white)

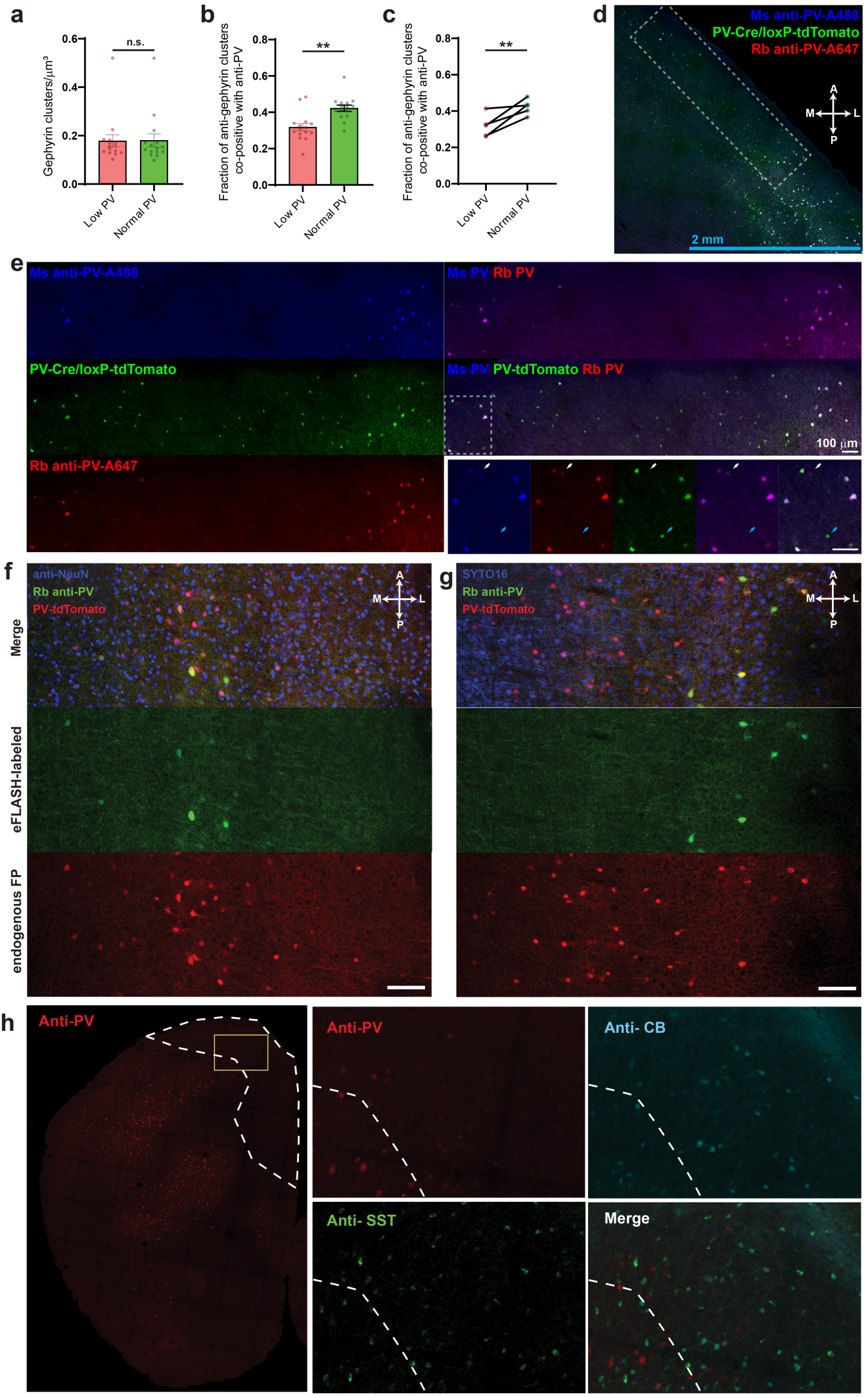

Extended Data Figure 7. Validation of low PV soma density regions. (**a-c**) Quantification of gephyrin clusters in low PV (red bars) and normal regions (green bars). (**a**) Density of gephyrin clusters. (**b-c**) Fraction of Gephyrin clusters co-positive with anti-PV, averaged in each ROI (**b**) and in each brain section (**c**). *N* = 5 animals. 3 ROIs each for low PV and normal regions per animal. One-Way ANOVA, n.s. = not significant, **P < 0.005. (**d-e**) Double passive immunolabeling of PV-Cre/*loxP*-tdTomato (green) mouse horizontal section with rabbit-host anti-PV (red) and mouse-host anti-PV (blue). (**e**) Magnified images from the marked box in **d**. In the inset, MsPV+/RbPV+/tdTomato- cell (white arrow) and MsPV-/RbPV-/tdTomato+ cell (cyan arrow). (**f-g**) Horizontal brain sections from PV-Cre/*loxP*-tdTomato (red) double transgenic mice eFLASH-immunolabeled with anti-PV (green) with additional round of passive labeling: (**f**) anti-NeuN (blue) and (**g**) SYTO16 (blue). (**h**) Passive immunolabeling of anti-PV (red), anti-CB (cyan), and anti-SST (green). Low PV region delineated with dotted white boundary. Scale bars = 2 mm (cyan) and 100 μm (white).

Supplementary Table 1 - Validated antibodies for eFLASH

Figure/Video title	Panel	Tissue Type	Target	Cat No	Conjugation	Company	Host/ Isotype	Clonality	Clone	Antibody conc. (µg/µl)	Primary Ab Volum Used	Secondary antibody (molar ratio and dye)
Figure 2	**e and f**	mouse brain hemisphere	NF (pan-axonal)	837904	-	Biolegend	Ms IgG1/IgM	P	SMI 312	0.5	10 µL	1:2 Fc-Fab A594
		mouse brain hemisphere	CB	13176BF	-	CST	Rb IgG	M	D1I4Q	2	1.5 µL	1:2 Fc-Fab SeTau647
Figure 3	**a**	rat whole brain	NeuN	24307S	-	CST	Rb IgG	M	D4G4O	-	50 µL	1:2 IgG SeTau647
	b	mouse whole brain	PV	PA1-933	-	Thermo	Rb IgG	P	-	1	10 µL	1:2 IgG SeTau647
	c	mouse brain hemisphere	NeuN	24307S	-	CST	Rb IgG	M	D4G4O	-	25 µL	1:2 Fc-Fab SeTau647
			TH	818001	-	Biolegend	Ms IgG2a	M	2/40/15	1	3 µL	1:2 Fc-Fab A594
			ChAT	AB144P	-	Millipore	Gt IgG	P	-	-	40 µL	1:2 Fc-Fab A488
	d	marmoset brain block	PV	PA1-933	-	Thermo	Rb IgG	P	-	1	25 µL	1:1.5 Fc-Fab SeTau647
	e	marmoset brain block	NPY	11976S	-	CST	Rb IgG	M	D7Y5A	0.17	20 µL	1:2.5 Fc-Fab RRX
	f	mouse embryo	Ret	AF482	-	R&D systems	Gt IgG	P	-	0.2	25 µL	1:2 Fc-Fab SeTau647
			Nf-M	MCA-3H11	-	Encor	Ms IgG1	M	3H11	1	5 µL	1:2 Fc-Fab SeTau647
Figure 4	**a**	mouse brain hemisphere	PV	PA1-933	-	Thermo	Rb IgG	P	-	1	10 µL	1:2 Fc-Fab SeTau647
	d	mouse brain hemisphere	ChAT	AB144P	-	Millipore	Gt IgG	P	-	-	40 µL	1:2 Fc-Fab SeTau647
Figure 5	**c**	mouse whole brain	CB	MCA-4H7	-	Encor	Ms IgG1	M	MCA-4H7	1	8 µL	1:2 Fc-Fab A594
			PV	PA1-933	-	Thermo	Rb IgG	P	-	1	8 µL	1:2 Fc-Fab SeTau647
	d	mouse whole brain	PV	PA1-933	-	Thermo	Rb IgG	P	-	1	10 µL	1:2 Fc-Fab SeTau647
Extended Data Figure 2	**a**	human cerebral organoid	Vimentin	9856S	A647	CST	Rb	M	D21H3	-	10 µL	-
			Tubulin β3	801208	A594	Biolegend	Ms IgG2a	M	TUJ1	0.5	1 µL	-
			SYTO 16	S7578	-	Thermo	-	-	-	-	5 µL	-
	b	human brain block	NPY	11976S	-	CST	Rb IgG	M	D7Y5A	0.17	30 µL	1:1.5 Fc-Fab SeTau647
	c	mouse liver lobule	Histone H3	ab237418	A647	abcam	Rb IgG	M	E191	0.5	40 µL	-
	d	mouse intestine	Tubulin β3	801201	-	Biolegend	Ms IgG2a	M	TUJ1	1	3 µL	1:2 Fc-Fab SeTau647
	e	mouse lung	a-SMA	C6198	Cy3	Millipore	Ms IgG2a	M	1A4	-	25 µL	-
			SYTO 16	S7578	-	Thermo	-	-	-	-	5 µL	-
	f	mouse ear canal	myosin VIIa	25-6790	-	Proteus	Rb IgG	P	-	-	2 µL	1:2 Fc-Fab SeTau647
	g	mouse heart	TH	AB512	-	Millipore	Rb IgG	P	-	-	25 µL	1:2 Fc-Fab SeTau647
			a-SMA	C6198	Cy3	Millipore	Ms IgG2a	M	1A4	-	25 µL	-
Extended Data Figure 3	**a**	mouse whole brain	NPY	11976S	-	CST	Rb IgG	M	D7Y5A	0.17	20 µL	1:2 Fc-Fab SeTau647
	b	mouse whole brain	CB	13176BF	-	CST	Rb IgG	M	D1I4Q	2	2.5 µL	1:2 Fc-Fab SeTau647
	c	mouse whole brain	ChAT	AB144P	-	Millipore	Gt IgG	P	-	-	60 µL	1:2 Fc-Fab SeTau647
	d	mouse whole brain	NF-M	MCA-3H11	-	Encor	Ms IgG1	M	3H11	1	30 µL	1:2.5 Fc-Fab RRX
	e	mouse whole brain	NeuN	24307	-	CST	Rb IgG	M	D4G4O	-	25 µL	1:2 Fc-Fab SeTau647
	f	mouse whole brain	TH	818001	-	Biolegend	Ms IgG2a	M	2/40/15	1	6 µL	1:2.5 Fc-Fab RRX
	g	mouse whole brain	VIP	ab227850	-	Abcam	Rb IgG	P	-	0.5	10 µL	1:2 IgG SeTau647
	h	mouse whole brain	SST	sc-47706	-	Santa Cruz	Rt IgG	M	YC7	0.2	25 µL	1:2.5 Fc-Fab RRX
	i	mouse whole brain	nNOS	ab1376	-	abcam	Gt IgG	P	-	0.5	6 µL	1:2 IgG SeTau647
	j	mouse brain hemisphere	IBA1	17198	-	CST	Rb IgG	M	E404W	-	8 µL	1:2 Fc-Fab SeTau647
	k	mouse brain hemisphere	GFAP	644708	A594	Biolegend	Ms IgG2b	M	2E1.E9	0.5	50 µL	-
	l	mouse brain hemisphere	TPH2	PA1-778	-	Thermo	Rb IgG	P	-	-	30 µL	1:2 Fc-Fab SeTau647
	m	mouse brain hemisphere	Lectin	DL-1177	Dy594	Vector Laboratories		-	-	-	50 µL	-
	n	mouse brain hemisphere	c-Fos	ab214672	-	abcam	Rb IgG	M	EPR20769	0.623	12 µL	1:2 Fc-Fab SeTau647
	o	mouse brain hemisphere	NF (pan-axonal)	837904	-	Biolegend	Ms IgG1/IgM	P	SMI 312	0.5	10 µL	1:2 Fc-Fab A594
	p	mouse brain hemisphere	CR	ab702	-	abcam	Rb IgG	P	-	-	50 µL	1:2 Fc-Fab SeTau647
	q	mouse brain hemisphere	SYTO 16	S7578	-	Thermo	-	-	-	-	6 µL	-
Supplementary Video 3		rat whole brain	NeuN	24307S	-	CST	Rb IgG	M	D4G4O	-	50 µL	1:2 IgG SeTau647
Supplementary Video 4		mouse whole brain	PV	PA1-933	-	Thermo	Rb IgG	P	-	1	10 µL	1:2 IgG SeTau647
Supplementary Video 5		mouse brain hemisphere	NeuN	24307S	-	CST	Rb IgG	M	D4G4O	-	25 µL	1:2 Fc-Fab SeTau647
			TH	818001	-	Biolegend	Ms IgG2a	M	2/40/15	1	3 µL	1:2 Fc-Fab A594
			ChAT	AB144P	-	Millipore	Gt IgG	P	-	-	40 µL	1:2 Fc-Fab A488
Supplementary Video 6		marmoset brain block	PV	PA1-933	-	Thermo	Rb IgG	P	-	1	25 µL	1:1.5 Fc-Fab SeTau647
		marmoset brain block	NPY	11976S	-	CST	Rb IgG	M	D7Y5A	0.17	20 µL	1:2.5 Fc-Fab RRX
Supplementary Video 7		mouse brain hemisphere	PV	PA1-933	-	Thermo	Rb IgG	P	-	1	10 µL	1:2 Fc-Fab SeTau647
Supplementary Video 8		mouse brain hemisphere	ChAT	AB144P	-	Millipore	Gt IgG	P	-	-	40 µL	1:2 Fc-Fab SeTau647
Supplementary Video 9		mouse whole brain	CB	MCA-4H7	-	Encor	Ms IgG1	M	MCA-4H7	1	8 µL	1:2 Fc-Fab A594
			PV	PA1-933	-	Thermo	Rb IgG	P	-	1	8 µL	1:2 Fc-Fab SeTau647
Supplementary Video 10		mouse whole brain	PV	PA1-933	-	Thermo	Rb IgG	P	-	1	10 µL	1:2 Fc-Fab SeTau647

Supplementary Table 1 - Validated antibodies for eFLASH

Target	Cat No	Conjugation	Company	Host/Isotype	Clonality	Clone	Conc (μg/μl)	Suggested antibody amount for whole mouse brain or organs
ALDH1A1	sc-166362	-	Santa Cruz	Ms IgG2b	M	H-8	-	3 μg
αSMA	ab5694	-	abcam	Rb IgG	P	-	0.2	5 μg
aSMA	C6198	Cy3	Millipore	Ms IgG2a	M	1A4	-	25 uL
β-amyloid	51374	-	CST	Rb IgG	M	-	N/A	30 μL
Calbindin	13176BF	-	CST	Rb IgG	M	D1I4Q	2	5 μg
Calbindin	13176S	-	CST	Rb IgG	M	D1I4Q	0.052	5 μg
Calbindin	ab108404	-	abcam	Rb IgG	M	EP3478	0.22	8 μg
Calbindin	MCA-4H7	-	Encor	Ms IgG1	M	MCA-4H7	1	5 μg
Calretinin	ab702	-	abcam	Rb IgG	P	-	-	50 μL
cFos	ab214672	-	abcam	Rb IgG	M	EPR20769	0.623	8 μg
cFos	RPCA-c-FOS	-	Encor	Rb IgG	P	-	1	5 μg
ChAT	AB144P	-	Millipore	Gt IgG	P	-	-	60 μL
CTIP2	ab18465	-	Abcam	Rt IgG	M	25B6	1	10 μg
CASP (Cux1)	ab54583	-	abcam	Ms IgG1	M	2A10	-	10 μg
GAD65/67	ab183999	-	abcam	Rb IgG	M	EPR19366	0.959	10 μg
GFAP	644708	A594	Biolegend	Ms IgG2b	M	2E1.E9	0.5	50 μL
GFAP	3657S	A647	CST	Ms IgG1	M	GA5	-	50 μL
GFAP	sc-58755	-	Santa Cruz	Ms IgG1	M	GA5	1	5 μg
GFP	GFP	-	Aves	Ch IgY	P	-	-	6 μg (Thy1-EGFP)
GFP	ab6658	Biotin	abcam	Gt IgG	P	-	1	5 μg (Thy1-EGFP)
Histone-H3	ab237418	A647	abcam	Rb IgG	M	E191	0.5	20 μg (Liver lobule)
Iba1	ab178847	-	Abcam	Rb IgG	M	EPR16589	0.632	10 μg
Iba1	17198	-	CST	Rb IgG	M	E404W	-	8 μg
MAP2	8707S	-	CST	Rb IgG	P	-	-	20 μL
mouse Ret	AF482	-	R&D systems	Gt IgG	P	-	0.2	5 μg (embryo)
Myelin Basic Protein	MCA-7G7	-	Encor	Ms IgG1	M	7G7	1	8 μg
Myelin Basic Protein	ab7349	-	abcam	Rt IgG	P	-	-	50 μL
Myo7a (Myosin VIIa)	25-6790	-	Proteus	Rb IgG	P	-	-	1 μg (inner ear)
Netrin-1	NET	-	Aves	Ch IgY	P	-	1	5 μg
NeuN	24307	-	CST	Rb IgG	M	D4G4O	-	50 μL
NeuN	36662	-	CST	Rb IgG	M	D4G4O	-	6 μg
NeuN	MAB377	-	Millipore	Ms IgG1	M	A60	1	10 μg
NeuN	MCA-1B7	-	Encor	Ms IgG2b,κ	M	1B7	1	10 μg
NeuN	834501	-	Biolegend	Ms IgG2b,κ	M	1B7	1	10 μg
NeuN	GPCA-Fox3	-	Encor	Gt IgG	P	-	1	20 μg
NeuN	RPCA-Fox3	-	Encor	Rb IgG	P	-	1	10 μg
Neurofilament-H	AB5539	-	Millipore	Ch IgY	P	-	-	3 μg (inner ear)
Neurofilament-H	801701	-	Biolegend	Ms IgG1	M	SMI 32	1	30 μg
Neurofilament-H	MCA-NAP4	-	Encor	Ms IgG1	M	NAP4	1	20 μg
Neurofilament-M	MCA-3H11	-	Encor	Ms IgG1	M	3H11	1	30 μg
Neurofilament-L	2835	-	CST	MS IgG1	M	DA2	-	20 μL
Neurofilament marker (pan-axonal)	837904	-	Biolegend	Ms IgG1/IgM	P	SMI 312	0.5	12 μg
nNos	ab1376	-	abcam	Gt IgG	P	-	0.5	3 μg
NPY	11976S	-	CST	Rb IgG	M	D7Y5A	0.17	3.5 μg
NPY	75-456	-	Neuromab	Ms IgG2a	M	L115/13	1	-
PDGFR1beta	ab32570	-	abcam	Rb IgG	P	-	-	5 μg
Phospho-Tau	MN1020	-	Invitrogen	Ms IgG1	M	-	0.2	-
PV	PA1-933	-	Thermo	Rb IgG	P	-	1	10 μg
PV	ab11427	-	abcam	Rb IgG	P	-	1	-
PV	MCA-3C9	-	Encor	Ms IgG1	M	3C9	1	-
PV	ab32895	-	abcam	Gt IgG	P	-	0.5	-
RFP	20422	CF594	Biotium	Rb IgG	P	-	1	expression-dependent
S100B	PA5-78161	-	Invitrogen	Rb IgG	P	-	1	5 μg
Sox2	5067	A647	CST	Rb IgG	M		0.025	0.5 μg (organoid)
SST	MAB354	-	Millipore	Rt IgG	M	YC7	-	50 μL
SST	sc-47706	-	Santa Cruz	Rt IgG	M	YC7	0.2	5 μg
SST	14-9751-82	-	eBioscience	Ms IgG1	M	ICDCLS	0.5	10 μg
TBR1	MA5-32564	-	Invitrogen	Rb IgG	M	-	1	10 μg
TBR1	66626	A594	CST	Rb IgG	M	D6C6X	0.1	0.5 μg (organoid)
TH	AB512	-	Millipore	Rb IgG	P	-	-	25 μL
TH	818001	-	Biolegend	Ms IgG2a	M	2/40/15	1	3 μg
TH	TYH	-	Aves	Ch IgY	P	-	0.2	6 μg
TPH2	PA1-778	-	Thermo	Rb IgG	P	-	-	30 μL
Tubulin β3	801201	-	Biolegend	Ms IgG2a	M	TUJ1	1	10 μg
Tubulin β3	801208	A594	Biolegend	Ms IgG2a	M	TUJ1	-	1 μg (organoid)
V5	A190-120A	-	Bethyl	Rb IgG	P	-	1	expression-dependent
Vimentin	sc-371717	-	Santa Cruz	Ms IgG1	M	-	0.2	8 μg
Vimentin	9854S	A488	CST	Rb	M	D21H3	-	1 μg (organoid)
Vimentin	9856S	A647	CST	Rb	M	D21H3	-	1 μg (organoid)
VIP	ab227850	-	Abcam	Rb IgG	P	-	0.5	10 μg
Goat anti-Chicken IgY, Fc fragmemt specific	103-547-008	A488	Jackson Immunoresearch	Gt Fab	P	-	-	
Goat anti-Chicken IgY, Fc fragmemt specific	103-297-008	RRX	Jackson Immunoresearch	Gt Fab	P	-	-	
Goat anti-Chicken IgY, Fc fragmemt specific	103-587-008	A594	Jackson Immunoresearch	Gt Fab	P	-	-	
Goat anti-Chicken IgY, Fc fragmemt specific	103-007-008	-	Jackson Immunoresearch	Gt Fab	P	-	-	
Goat anti-Chicken IgY, Fc fragmemt specific	conj. in house	SeTau647	Jackson Immunoresearch	Gt Fab	P	-	-	
Goat anti-Mouse IgG1, Fcγ fragmemt specific	115-547-185	A488	Jackson Immunoresearch	Gt Fab	P	-	-	
Goat anti-Mouse IgG1, Fcγ fragmemt specific	115-297-185	RRX	Jackson Immunoresearch	Gt Fab	P	-	-	
Goat anti-Mouse IgG1, Fcγ fragmemt specific	115-587-185	A594	Jackson Immunoresearch	Gt Fab	P	-	-	
Goat anti-Mouse IgG1, Fcγ fragmemt specific	115-607-185	A647	Jackson Immunoresearch	Gt Fab	P	-	-	
Goat anti-Mouse IgG1, Fcγ fragmemt specific	115-007-185	-	Jackson Immunoresearch	Gt Fab	P	-	-	
Goat anti-Mouse IgG1, Fcγ fragmemt specific	conj. in house	SeTau647	Jackson Immunoresearch	Gt Fab	P	-	-	
Goat anti-Mouse IgG2a, Fcγ fragmemt specific	115-297-186	RRX	Jackson Immunoresearch	Gt Fab	P	-	-	
Goat anti-Mouse IgG2a, Fcγ fragmemt specific	115-587-186	A594	Jackson Immunoresearch	Gt Fab	P	-	-	
Goat anti-Mouse IgG2a, Fcγ fragmemt specific	115-007-186	-	Jackson Immunoresearch	Gt Fab	P	-	-	
Goat anti-Mouse IgG2a, Fcγ fragmemt specific	conj. in house	SeTau647	Jackson Immunoresearch	Gt Fab	P	-	-	
Goat anti-Mouse IgG2b, Fcγ fragmemt specific	115-297-187	RRX	Jackson Immunoresearch	Gt Fab	P	-	-	
Goat anti-Mouse IgG2b, Fcγ fragmemt specific	115-587-187	A594	Jackson Immunoresearch	Gt Fab	P	-	-	
Goat anti-Mouse IgG2b, Fcγ fragmemt specific	115-007-187	-	Jackson Immunoresearch	Gt Fab	P	-	-	
Goat anti-Mouse IgG2b, Fcγ fragmemt specific	conj. in house	SeTau647	Jackson Immunoresearch	Gt Fab	P	-	-	
Goat anti-Rabbit IgG, Fc fragmemt specific	111-547-008	A488	Jackson Immunoresearch	Gt Fab	P	-	-	
Goat anti-Rabbit IgG, Fc fragmemt specific	111-297-008	RRX	Jackson Immunoresearch	Gt Fab	P	-	-	
Goat anti-Rabbit IgG, Fc fragmemt specific	111-587-008	A594	Jackson Immunoresearch	Gt Fab	P	-	-	
Goat anti-Rabbit IgG, Fc fragmemt specific	111-607-008	A647	Jackson Immunoresearch	Gt Fab	P	-	-	
Goat anti-Rabbit IgG, Fc fragmemt specific	111-007-008	-	Jackson Immunoresearch	Gt Fab	P	-	-	
Goat anti-Rabbit IgG, Fc fragmemt specific	conj. in house	SeTau647	Jackson Immunoresearch	Gt Fab	P	-	-	
Goat anti-Rat IgG, Fcγ fragmemt specific	112-547-008	A488	Jackson Immunoresearch	Gt Fab	P	-	-	
Goat anti-Rat IgG, Fcγ fragmemt specific	112-297-008	RRX	Jackson Immunoresearch	Gt Fab	P	-	-	
Goat anti-Rat IgG, Fcγ fragmemt specific	112-587-008	A594	Jackson Immunoresearch	Gt Fab	P	-	-	
Goat anti-Rat IgG, Fcγ fragmemt specific	112-007-008	-	Jackson Immunoresearch	Gt Fab	P	-	-	
Goat anti-Rat IgG, Fcγ fragmemt specific	conj. in house	SeTau647	Jackson Immunoresearch	Gt Fab	P	-	-	
Bovine anti-Goat IgG, Fc fragmemt specific	805-547-008	A488	Jackson Immunoresearch	Bo Fab	P	-	-	
Bovine anti-Goat IgG, Fc fragmemt specific	805-297-008	RRX	Jackson Immunoresearch	Bo Fab	P	-	-	
Bovine anti-Goat IgG, Fc fragmemt specific	805-587-008	A594	Jackson Immunoresearch	Bo Fab	P	-	-	
Bovine anti-Goat IgG, Fc fragmemt specific	805-007-008	-	Jackson Immunoresearch	Bo Fab	P	-	-	
Bovine anti-Goat IgG, Fc fragmemt specific	conj. in house	SeTau647	Jackson Immunoresearch	Bo Fab	P	-	-	
Donkey anti-Mouse IgG H&L	ab150109	A488	Abcam	Dn IgG	P	-	2	
Donkey anti-Mouse IgG H&L	ab175700	A568	Abcam	Dn IgG	P	-	2	
Donkey anti-Mouse IgG H&L	ab150111	A647	Abcam	Dn IgG	P	-	2	
Donkey anti-Rabbit IgG H&L	ab150061	A488	Abcam	Dn IgG	P	-	2	
Donkey anti-Rabbit IgG H&L	ab175693	A568	Abcam	Dn IgG	P	-	2	
Donkey anti-Rabbit IgG H&L	ab150063	A647	Abcam	Dn IgG	P	-	2	
Donkey anti-Goat IgG H&L	ab150133	A488	Abcam	Dn IgG	P	-	2	
Donkey anti-Goat IgG H&L	ab175704	A568	Abcam	Dn IgG	P	-	2	
Donkey anti-Goat IgG H&L	ab150135	A647	Abcam	Dn IgG	P	-	2	
Goat anti-Chicken IgY H&L	ab150173	A488	Abcam	Dn IgG	P	-	2	
Goat anti-Chicken IgY H&L	ab175711	A568	Abcam	Dn IgG	P	-	2	
Goat anti-Chicken IgY H&L	ab150175	A647	Abcam	Dn IgG	P	-	2	
Streptavidin-647	S21374	A647	Thermo	-	-	-	-	
lectin	DL-1177	Dy594	Vector Laboratories	-	-	-	1	
SYTO16	S7578	-	Thermo	-	-	-	1mM	

Supplementary Table 2 - Imaging conditions

Sample Type	Labeling	Associated figure	Associated supplementary video	Microscope	Objective	Objective immersion media	Sample mounting media	Z-step size	Bit depth	Post processing		
										De-striping	Stitching	Illumination correction
Mouse tissue sections	Anti-NPY, Anti-PV	Fig 2a-b	-	Leica TCS SP8	20X 0.5 NA water-immersion, HCX APO L U-V-I	DI water	PBST	<1µm	12	no	no	no
Mouse brain hemisphere	anti-CB, anti-NF(SMI312), SYTO16	Fig 2e, ExFig 2f	Svideo 2	SmartSPIM, LifeCanvas	3.6x objective (custom lifecanvas design, 0.2NA lateral resolution 1.8µm in XY)	EasyIndex	EasyIndex	2µm	16	yes	yes	yes
Mouse brain hemisphere	anti-CB, anti-NF(SMI312), SYTO16	Fig 2f, ExFig 2f	Svideo 2	SmartSPIM, LifeCanvas	3.6x objective (custom lifecanvas design, 0.2NA lateral resolution 1.8µm in XY)	EasyIndex	EasyIndex	2µm	16	yes	yes	yes
Mouse whole brain	anti-PV	Fig 3a	Svideo 3	SmartSPIM, LifeCanvas	3.6x objective (custom lifecanvas design, 0.2NA lateral resolution 1.8µm in XY)	EasyIndex	EasyIndex	2µm	16	yes	yes	yes
Mouse brain hemisphere	anti-NeuN, anti-TH, anti-ChAT	Fig 3b	Svideo 4	SmartSPIM, LifeCanvas	3.6x objective (custom lifecanvas design, 0.2NA lateral resolution 1.8µm in XY)	EasyIndex	EasyIndex	2µm	16	yes	yes	yes
Rat whole brain	anti-NeuN	Fig 3c	Svideo 5	SmartSPIM, LifeCanvas	3.6x objective (custom lifecanvas design, 0.2NA lateral resolution 1.8µm in XY)	EasyIndex	EasyIndex	4µm	16	yes	yes	yes
Marmoset brain block	anti-PV	Fig 3d	Svideo 6	SmartSPIM, LifeCanvas	3.6x objective (custom lifecanvas design, 0.2NA lateral resolution 1.8µm in XY)	EasyIndex	EasyIndex	2µm	16	yes	yes	yes
Marmoset brain block	anti-NPY	Fig 3e	Svideo 6	SmartSPIM, LifeCanvas	10X 0.6 NA CLARITY-optimized, XLPLN10XSVMP (laternal resolution 0.65µm in XY)	EasyIndex	EasyIndex	1µm	16	yes	yes	yes
Mouse embryo	anti-mouse Ret, anti-NF-M	Fig 3f	-	SmartSPIM, LifeCanvas	3.6x objective (custom lifecanvas design, 0.2NA lateral resolution 1.8µm in XY)	EasyIndex	EasyIndex	2µm	16	yes	yes	yes
Human cerebral organoid	anti-Vimentin, anti-β-tubulin, SYTO16	ExFig3	-	Leica TCS SP8	20X 0.5 NA water-immersion, HCX APO L U-V-I	EasyIndex	EasyIndex	<1µm	16	no	yes	no
Human brain block	anti-NPY	ExFig3	-	SmartSPIM, LifeCanvas	3.6x objective (custom lifecanvas design, 0.2NA lateral resolution 1.8µm in XY)	EasyIndex	EasyIndex	4µm	16	yes	yes	yes
Mouse livery lobule	anti-His-H3	ExFig3	-	SmartSPIM, LifeCanvas	3.6x objective (custom lifecanvas design, 0.2NA lateral resolution 1.8µm in XY)	EasyIndex	EasyIndex	2µm	16	yes	yes	yes
Mouse intestine	ChAT(BAC)-eGFP, Anti-Tubulin β3	ExFig3	-	SmartSPIM, LifeCanvas	3.6x objective (custom lifecanvas design, 0.2NA lateral resolution 1.8µm in XY)	EasyIndex	EasyIndex	2µm	16	yes	yes	yes
Mouse lung	anti-αSMA	ExFig3	-	SmartSPIM, LifeCanvas	3.6x objective (custom lifecanvas design, 0.2NA lateral resolution 1.8µm in XY)	EasyIndex	EasyIndex	2µm	16	yes	yes	yes
Mouse ear canal	anti-Myosin VIIa, Thy1-EGFP	ExFig3	-	Leica TCS SP8	20X 0.5 NA water-immersion, HCX APO L U-V-I	EasyIndex	EasyIndex	<1µm	16	no	yes	no
Mouse heart	anti-αSMA, anti-TH	ExFig3	-	SmartSPIM, LifeCanvas	3.6x objective (custom lifecanvas design, 0.2NA lateral resolution 1.8µm in XY)	EasyIndex	EasyIndex	2µm	16	yes	yes	yes
Mouse whole brain	anti-NPY	ExFig4	-	SmartSPIM, LifeCanvas	3.6x objective (custom lifecanvas design, 0.2NA lateral resolution 1.8µm in XY)	EasyIndex	EasyIndex	2µm	16	yes	yes	yes
Mouse whole brain	anti-CB	ExFig4	-	SmartSPIM, LifeCanvas	3.6x objective (custom lifecanvas design, 0.2NA lateral resolution 1.8µm in XY)	EasyIndex	EasyIndex	2µm	16	yes	yes	yes
Mouse whole brain	anti-ChAT	ExFig4	-	SmartSPIM, LifeCanvas	3.6x objective (custom lifecanvas design, 0.2NA lateral resolution 1.8µm in XY)	EasyIndex	EasyIndex	2µm	16	yes	yes	yes
Mouse whole brain	anti-NF-M	ExFig4	-	SmartSPIM, LifeCanvas	3.6x objective (custom lifecanvas design, 0.2NA lateral resolution 1.8µm in XY)	EasyIndex	EasyIndex	2µm	16	yes	yes	yes
Mouse whole brain	anti-NeuN	ExFig4	-	SmartSPIM, LifeCanvas	3.6x objective (custom lifecanvas design, 0.2NA lateral resolution 1.8µm in XY)	EasyIndex	EasyIndex	2µm	16	yes	yes	yes
Mouse whole brain	Anti-TH	ExFig4	-	SmartSPIM, LifeCanvas	3.6x objective (custom lifecanvas design, 0.2NA lateral resolution 1.8µm in XY)	EasyIndex	EasyIndex	2µm	16	yes	yes	yes
Mouse brain hemisphere	Anti-NPY, Anti-SST	ExFig4, ExFig5	-	SmartSPIM, LifeCanvas	3.6x objective (custom lifecanvas design, 0.2NA lateral resolution 1.8µm in XY)	EasyIndex	EasyIndex	2µm	16	yes	yes	yes
Mouse brain hemisphere	AntiTH, Anti-TPH2	ExFig4, ExFig5	-	SmartSPIM, LifeCanvas	3.6x objective (custom lifecanvas design, 0.2NA lateral resolution 1.8µm in XY)	EasyIndex	EasyIndex	2µm	16	yes	yes	yes
Mouse brain hemisphere	Anti-cFos	ExFig3, ExFig4		SmartSPIM, LifeCanvas	3.6x objective (custom lifecanvas design, 0.2NA lateral resolution 1.8µm in XY)	EasyIndex	EasyIndex	2µm	16	yes	yes	yes
Mouse brain hemisphere	Anti-Iba1	ExFig3, ExFig4	-	SmartSPIM, LifeCanvas	3.6x objective (custom lifecanvas design, 0.2NA lateral resolution 1.8µm in XY)	EasyIndex	EasyIndex	2µm	16	yes	yes	yes
Mouse brain hemisphere	Anti-GFAP, lectin	ExFig3, ExFig4	-	SmartSPIM, LifeCanvas	3.6x objective (custom lifecanvas design, 0.2NA lateral resolution 1.8µm in XY)	EasyIndex	EasyIndex	2µm	16	yes	yes	yes
Mouse brain hemisphere	anti-PV, anti-SMI312, SYTO16	ExFig3, ExFig4	-	SmartSPIM, LifeCanvas	3.6x objective (custom lifecanvas design, 0.2NA lateral resolution 1.8µm in XY)	EasyIndex	EasyIndex	2µm	16	yes	yes	yes
Mouse brain hemisphere	Anti-CR	ExFig3, ExFig4	-	SmartSPIM, LifeCanvas	3.6x objective (custom lifecanvas design, 0.2NA lateral resolution 1.8µm in XY)	EasyIndex	EasyIndex	2µm	16	yes	yes	yes
Mouse brain hemisphere	Anti-ChAT	ExFig3, ExFig4	-	SmartSPIM, LifeCanvas	3.6x objective (custom lifecanvas design, 0.2NA lateral resolution 1.8µm in XY)	EasyIndex	EasyIndex	2µm	16	yes	yes	yes
Mouse brain hemisphere	PV-Cre/loxP-tdTomato, anti-PV	Fig 4a-c	Svideo 7	SmartSPIM, LifeCanvas	3.6x objective (custom lifecanvas design, 0.2NA lateral resolution 1.8µm in XY)	EasyIndex	EasyIndex	2µm	16	yes	yes	yes
Mouse brain hemisphere	ChAT(BAC)-eGFP, Anti-ChAT	Fig 4d-h	Svideo 8	SmartSPIM, LifeCanvas	3.6x objective (custom lifecanvas design, 0.2NA lateral resolution 1.8µm in XY)	EasyIndex	EasyIndex	2µm	16	yes	yes	yes
Mouse tissue sections	anti-PV, DAPI	ExFig 5b-c	-	Leica TCS SP8	20X 0.5 NA water-immersion, HCX APO L U-V-I	DI water	EasyIndex	4µm	12	no	no	no
Mouse tissue sections	PV-Cre/loxP-tdTomato, anti-PV	Fig 5b, ExFig 6d-e	-	Leica TCS SP8	20X 0.5 NA water-immersion, HCX APO L U-V-I	DI water	PBST	<1µm	12	no	no	no
Mouse tissue sections	anti-PV, anti-Gephyrin, anti-NeuN	Fig 5b-i-ii	-	Leica TCS SP8	63X 1.20 NA water-immersion, HC PC APO CORR CS2	DI water	PBST	<1µm	12	no	no	no
Mouse tissue sections	PV-Cre/loxP-tdTomato, anti-PV	ExFig 6f	-	Leica TCS SP8	20X 0.5 NA water-immersion, HCX APO L U-V-I	DI water	PBST	<1µm	12	no	no	no
Mouse tissue sections	PV-Cre/loxP-tdTomato, anti-PV	ExFig 6g	-	Leica TCS SP8	20X 0.5 NA water-immersion, HCX APO L U-V-I	DI water	PBST	<1µm	12	no	no	no
Mouse tissue sections	anti-PV, anti-CB, anti-SST	Fig 5b-i-ii	-	Leica TCS SP8	20X 0.5 NA water-immersion, HCX APO L U-V-I	DI water	PBST	<1µm	12	no	no	no
Mouse whole brain	anti-CB, anti-PV	Fig 5c	Svideo 9	SmartSPIM, LifeCanvas	3.6x objective (custom lifecanvas design, 0.2NA lateral resolution 1.8µm in XY)	EasyIndex	EasyIndex	2µm	16	yes	yes	no
Mouse whole brain	PV-Cre/loxP-tdTomato, anti-PV	Fig 5c	Svideo 10	SmartSPIM, LifeCanvas	3.6x objective (custom lifecanvas design, 0.2NA lateral resolution 1.8µm in XY)	EasyIndex	EasyIndex	2µm	16	yes	yes	yes

Parvalbumin

Rb PA1-933 (Thermo) | Ms MCA-3C9 (Encor) | Overlay

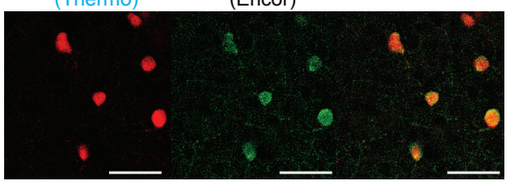

Rb ab11427 (Abcam) | Ms 235 (Swant) | Overlay

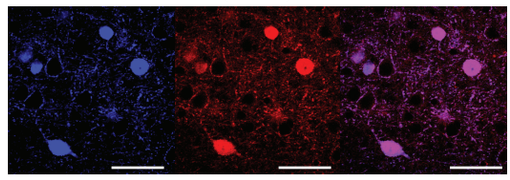

Neuropeptide-Y

Rb 11976S (CST) | Ms 75-456 (NeuroMab) | Overlay

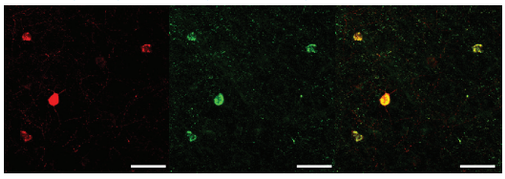

Calbindin

Rb 13176S (CST) | Ms MCA-4H7 (Encor) | Overlay

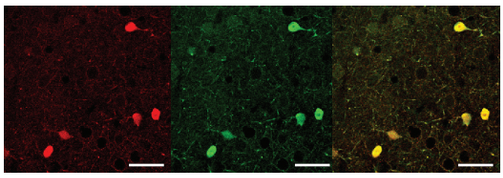

Rb ab108404 (abcam) | Ms MCA-4H7 (Encor) | Overlay

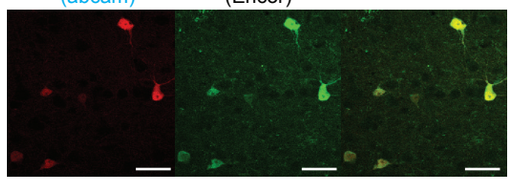

Calretinin

Rb ab702 (Abcam) | Ms 6B3 (Swant) | Go CG1 (Swant) | Overlay

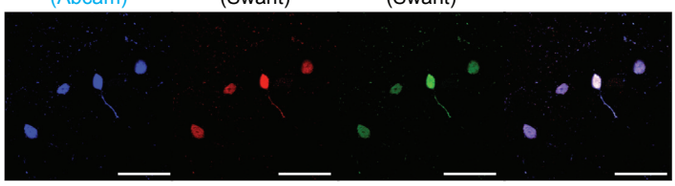

Somatostatin

Rt MAB354 (CST) | Ms 14-9751-82 (eBioscience) | Overlay

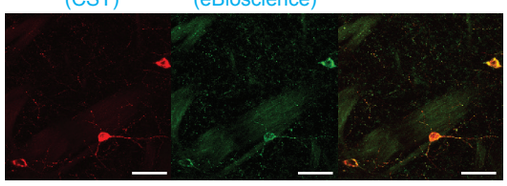

Rt sc-47706 (Santa Cruz) | Ms 14-9751-82 (eBioscience) | Overlay

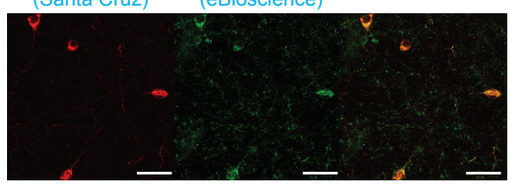

Tyrosine Hydroxylase

Rb ab112 (Abcam) | Ms 808001 (Biolegend) | Ch TH (Aves) | Overlay

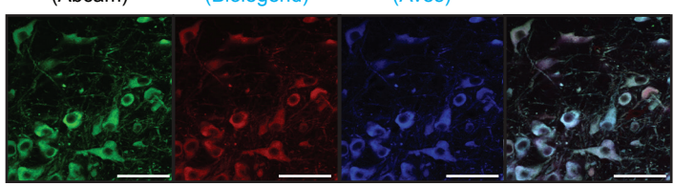

NeuN

Rb 24307S (CST) | Ms MCA-1B7 (Encor) | Overlay

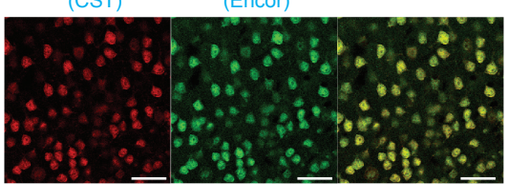

Rb 12943S (CST) | Ms MAB377 (Millipore) | Overlay

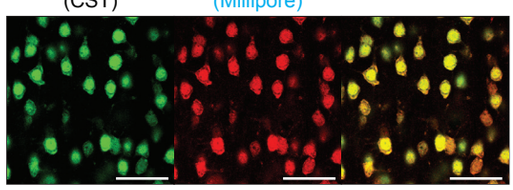

MBP

Rt ab7349 (Abcam) | Ch ab134018 (Abcam)

Smi312

Ms 837904 (Biolegend) | Overlay

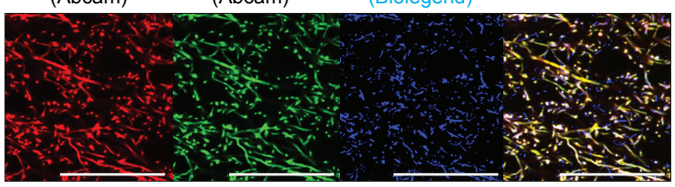

Supplementary Figure 1. Antibody validation by co-staining a tissue with multiple antibodies targeting the same antigen. Antibodies used for eFLASH staining are marked in light blue. For SMI-312 antibody, because only mouse-host SMI-312 antibodies are available, we co-stained a tissue with SMI-312 and myelin basic protein antibody, both of which target axon. Scale bar = 50 μm.

Supplementary Video 1. Computational modeling of implementing CuRVE for volumetric immunolabeling. Initial condition at T = 0: 20 mm spherical tissue with uniform distribution of antigen in a cylindrical container with aqueous solution enriched with antibodies. (**a-b**) Volumetric heatmap of antibody-antigen complex concentration throughout the experiment with (**a**) traditional approach with static binding strength and (**b**) CuRVE approach with swept binding strength. (**c-d**) Volumetric heatmap of unbound antibody concentration throughout the experiment with (**c**) traditional approach and (**d**) CuRVE approach.

Supplementary Video 2. Comparison of volumetric immunolabeling with SE and eFLASH. Two hemispheres from the same mouse are labeled using the same amount of antibodies: 3 μg of anti-Calbindin (CB, cyan) and 5 μg of anti-Neurofilament marker SMI-312 (NF, magenta). SE-labeled (left). eFLASH-labeled (right). The video shows optical section flythrough of intact mouse hemispheres in sagittal plane. Video also pans through cortex, hippocampus, striatum, and cerebellum.

Supplementary Video 3. Volumetric immunolabeling of whole rat brain with eFLASH. Optical section flythrough (horizontal plane) of whole rat brain labeled with anti-neuronal nuclei (NeuN, cyan) using eFLASH. (**a-c**) magnified regions.

Supplementary Video 4. Volumetric immunolabeling of whole mouse brain with eFLASH. Optical section flythrough (horizontal plane) of whole mouse brain labeled with anti-Parvalbumin (PV, white) antibody using eFLASH.

Supplementary Video 5. Volumetric triple immunolabeling of intact mouse hemisphere with eFLASH. Optical section flythrough (sagittal plane) of intact mouse hemisphere labeled with anti-neuronal nuclei (NeuN, cyan), anti-cholinergic acetyltransferase (ChAT, magenta), and anti-tyrosine hydroxylase (TH, yellow) using eFLASH. (**a-c**) magnified regions.

Supplementary Video 6. Multi-round volumetric immunolabeling of marmoset visual with eFLASH. Optical section flythrough (coronal plane) of marmoset brain block (5 mm x 5 mm x 8 mm) containing visual cortex labeled with anti-parvalbumin (PV, cyan) then anti-neuropeptide Y (NPY, cyan) using eFLASH. Anti-PV was stripped before the tissue was labeled again with anti-NPY.

Supplementary Video 7. Volumetric immunolabeling of PV-Cre/*loxP*-tdTomato double transgenic reporter mouse hemisphere with eFLASH. Optical section flythrough (sagittal plane) of intact mouse hemisphere expressing fluorescent protein (tdTomato, red) labeled with anti-parvalbumin (PV, green) using eFLASH. Followed by magnified panning through frontal pole of cerebral cortex, reticular nucleus of the thalamus, and ventral striatum.

Supplementary Video 8. Volumetric immunolabeling of ChAT^{BAC}eGFP transgenic reporter mouse hemisphere with eFLASH. Volumetric rending followed by optical section flythrough (sagittal plane) of intact mouse hemisphere expressing fluorescent protein (EGFP, green) labeled with anti-choline acetyltransferase (ChAT, green) using eFLASH. Followed by magnified panning through striatum, hippocampus, somatosensory cortex, hindbrain, and medulla.

Supplementary Video 9. eFLASH volumetric immunolabeling of wildtype mouse whole brain with regionalized loss of parvalbumin immunoreactive cells. Optical section flythrough (horizontal plane) of intact mouse whole brain labeled with anti-Calbindin (CB, magenta) and anti-parvalbumin (PV, cyan) using eFLASH. (**a-c**) Magnified regions with low PV soma density in anti-PV (cyan) channel indicated by white arrows.

Supplementary Video 10. eFLASH volumetric immunolabeling of PV-Cre/*loxP*-tdTomato double transgenic reporter mouse whole brain with regionalized loss of parvalbumin immunoreactive cells. Optical section flythrough (horizontal plane) of intact mouse whole brain expressing fluorescent protein (tdTomato, magenta) labeled with anti-parvalbumin (PV, cyan) using eFLASH. (**a-c**) Magnified regions with low PV soma density in anti-PV (cyan) channel indicated by white arrows.

Supplementary Notes: COMSOL modeling of diffusion-reaction kinetics of monoclonal antibody

We performed COMSOL simulation to assess the impact of Continuous Redispersion of Volumetric Equilibrium (CuRVE) in tortuous medium for volumetric immunolabeling. Briefly, CuRVE describes a paradigm where the change in tissue chemical environment occurs at a rate slow enough to allow the redispersion of unevenly distributed chemicals, thereby reestablishing chemical equilibrium tissue-wide at any given moment. The goal of the simulation is to compare two modes: one with static antibody reaction kinetics, and another with gradually modulated reaction kinetics that approximate the effect of CuRVE.

For the COMSOL simulation, the geometry of a biological tissue was simplified as a sphere of radius R. The modeling equation and parameters are adapted from Graff and Wittrup (2003)[1]. The reaction of antibodies with antigen inside the biological tissue can be simplified into the following reversible chemical formula[2]:

$$\mathrm{Antibody} + \mathrm{Antigen} \rightleftharpoons \mathrm{Complex}$$

Using chemical conservation equation, we can set up material balances for antibody and antigen within biological tissues.

$$\frac{\partial \mathrm{C}_{Ab}}{\partial \mathrm{t}} = \mathrm{D}_{eff} \nabla^2 \mathrm{C}_{Ab} + R_V$$

$$\frac{\partial \mathrm{C}_{Ag}}{\partial \mathrm{t}} = R_V$$

C_{Ab} and C_{Ab} denote the concentrations of the antibody and antigen respectively. D_{eff} is the effective diffusion coefficient and R_V is the volumetric antibody-antigen reaction rate within the tissue. To simplify our simulation, we assumed a uniform antigen concentration profile within the tissue. The sample container was chosen to be a cylindrical shape with height and radius proportional to the tissue, in which antibody is uniformly dispersed in the buffer, initially occupying outer space of the tissue sphere.

For other kinetic parameters, we adapted the values referenced from existing literature, and the parameters and variables are tabulated in Table 1. Particularly, we used faster effective diffusivity in our simulation of stochastic electrotransport, with the order of $10^{-8} m^2 s^{-1}$. The antibody-antigen reaction rate expression was a second order kinetics with following expression:

$$R_{forward} = -k_{on} C_{Ag} C_{Ab}$$

To minimize the numerical noise due to the step change in antigen concentration, we applied an adaptive mesh setting on the edge of the tissue by adding boundary layers. The simulation time span was 1 day total. The simulations were carried out in low antibody regime (Ab/Ag < 1) as full saturation of antigens is not a scalable approach. Both the static and the swept reaction modes shared identical parameters except the association rate constant, k_{on}, whose modulation approximates the effect of the changing chemical

environment on antibody binding kinetics. For the swept reaction mode, k_{on} parameter was modulated quadratically with the following expression:

$$k_{on,swept}(t) = 0.25 \times k_{on}\left(\frac{t}{t_{span}}\right)^2$$

For the static reaction mode, following expression as used:

$$k_{on,static}(t) = 0.3 \times k_{on}$$

To compare the sensitivity of both reaction modes, parametric sweep was performed for Ag_0, k_D(k_{off}/k_{on}), Ab_0/Ag_0, and R, representing variabilities in antigen density, antibody kinetics, antibody titration, and tissue thickness. The values used for the parametric sweeps are also tabulated in Table 1.

Table 1. Table of simulation parameters and their descriptions

Parameters	Description	Value	For Parametric Sweep	References
Ab_0	Initial antibody conc.	$Ag_0 \times \frac{V_{tissue}}{V_{cont} - V_{tissue}}$	See Ratio parameter below	—
Ag_0	Initial antigen conc.	$1.5 \times 10^{-8} M$	4.74e-10, 1.5e-9, 4.74e-9, 1.5e-8, 4.74e-8, 1.5e-7	1
D_{eff}	Effective diffusivity	$3 \times 10^{-9}\ m^2/s$	—	1,3,4
$D_{eff\_passive}$	Effective diffusivity (simple diffusion)	$3 \times 10^{-11}\ m^2/s$	—	5
K_D	Equilibrium dissociation constant	$1 \times 10^{-10}\ M$	10^{-7}, 10^{-8}, 10^{-9}, 10^{-10}, 10^{-11}, 10^{-12}	1,6
k_{off}	Dissociation rate const.	$1 \times 10^{-5} s^{-1}$	$10^{-3.5}$, 10^{-4}, $10^{-4.5}$, 10^{-5}, $10^{-5.5}$, 10^{-6}	1,6
k_{on}	Association rate const.	$1 \times 10^{-5} M^{-1} s^{-1}$	$10^{3.5}$, 10^{4}, $10^{4.5}$, 10^{5}, $10^{5.5}$, 10^{6}	1,6
Ratio	Ratio of antibody/antigen	0.3	0.1, 0.3, 0.5, 0.7, 0.9, 1.1	—
h_{cont}	Height of container	$2 \times (R \times 1.05)$	—	—
R_{cont}	Radius of container	$R \times 1.05$	—	—
R	Radius of biological tissue	10 mm	2.5, 5, 7.5, 10, 12.5, 15	—

1. Graff, C. P. & Wittrup, K. D. Theoretical analysis of antibody targeting of tumor spheroids: importance of dosage for penetration, and affinity for retention. *Cancer Res* **63**, 1288–96 (2003).

2. Reverberi, R. & Reverberi, L. Factors affecting the antigen-antibody reaction. *Blood Transfusion* **5**, 227 (2007).

3. Kim, S.-Y. *et al.* Stochastic electrotransport selectively enhances the transport of highly electromobile molecules. *Proceedings of the National Academy of Sciences* **112**, E6274–E6283 (2015).

4. Saltzman, W. M., Radomsky, M. L., Whaley, K. J. & Cone, R. A. Antibody diffusion in human cervical mucus. *Biophys J* **66**, 508–515 (1994).

5. Pokrić, B. & Pučar, Z. The two-cross immunodiffusion technique: Diffusion coefficients and precipitating titers of IgG in human serum and rabbit serum antibodies. *Anal Biochem* **93**, 103–114 (1979).

6. Landry, J. P., Ke, Y., Yu, G. L. & Zhu, X. D. Measuring Affinity Constants of 1,450 Monoclonal Antibodies to Peptide Targets with a Microarray-based Label-Free Assay Platform. *J Immunol Methods* **417**, 86 (2015).